Discontinuity-induced bifurcations in a piecewise-smooth capsule system with bidirectional drifts

Bingyong Guo[a,b], Joseph Páez Chávez[c,e], Yang Liu[b,*], Caishan Liu[d]

[a] *School of Marine Science and Technology, Northwestern Polytechnical University, Xi'an, Shaanxi 710072, China*
[b] *College of Engineering, Mathematics and Physical Sciences, University of Exeter, North Park Rd, Exeter, EX4 4QF, UK*
[c] *Center for Applied Dynamical Systems and Computational Methods (CADSCOM), Faculty of Natural Sciences and Mathematics, Escuela Superior Politécnica del Litoral, P.O. Box 09-01-5863, Guayaquil, Ecuador*
[d] *State Key Laboratory for Turbulence and Complex Systems, College of Engineering, Peking University, Beijing, 100871, China*
[e] *Center for Dynamics, Department of Mathematics, TU Dresden, D-01062 Dresden, Germany*

Abstract

Discontinuous friction and impact exist in a variety of piecewise-smooth dynamical systems that exhibit rich and complex nonlinear phenomena. This paper aims to study the discontinuity-induced grazing and adding-sliding bifurcations in a piecewise-smooth capsule system subjected to bidirectional drifts. For this purpose, analytical and semi-analytical onset conditions of the impact-induced grazing and the friction-induced adding-sliding bifurcations are investigated by solving explicitly the underlying piecewise-linear model. In this way, parametric relations revealing the occurrence mechanisms of transitions of the system from stationary to forward progression can be derived. This analytical approach is verified numerically using path-following techniques for piecewise-smooth dynamical systems. The numerical investigation includes a parametric study of the observed average capsule velocity and power consumption suggesting optimal choices for system operation.

Keywords: Piecewise-smooth dynamical system; Discontinuity-induced bifurcation; Grazing bifurcation; Adding-sliding bifurcation; Semi-analytical method

1. Introduction

Vibro-impact systems appear naturally in a broad variety of engineering applications, such as drilling [1, 2], moling [3], nonlinear energy sink [4, 5], energy harvesting [6, 7] and medical diagnosis [8, 9]. Fig. 1 presents four typical vibro-impact systems that were studied extensively in the past decade, including the impact oscillator [10], the vibro-impact nonlinear energy sink [5], the drifting oscillator with unidirectional drift [11] and the vibro-impact capsule system with bidirectional drifts [12]. In these systems, the common feature is that they experience impact and friction which induce discontinuity in their dynamics, resulting in rich and complex nonlinear phenomena, such as grazing [13–15] and sliding bifurcations [16, 17], chaotic motions [12, 18, 19] and coexistence [20, 21]. Due to the friction- and impact-induced discontinuities, bifurcation theory, mapping techniques and numerical analysis were widely applied to study system behaviours under parameter variations, to optimise system design, or to control system response.

The development of analytical methods to understand vibro-impact systems has played a major role in their study and experimental realization, as shown in a series of previous investigations [11, 22–29]. For a single degree-of-freedom (DoF) vibro-impact system, degenerate grazing bifurcation points of $1/n$ impact periodic motions were analytically determined in [23]. For a two-DoFs plastic vibro-impact system, the existence and stability of period-n-1-impact motions were derived analytically in [24]. Analytical studies with multiple scales method was conducted in [25, 26] to predict slow invariant manifolds or

*Corresponding author. Tel: +44(0)1392-724654, e-mail: y.liu2@exeter.ac.uk.
Email addresses: b.guo@exeter.ac.uk (Bingyong Guo), jpaez@espol.edu.ec (Joseph Páez Chávez), liucs@pku.edu.cn (Caishan Liu)

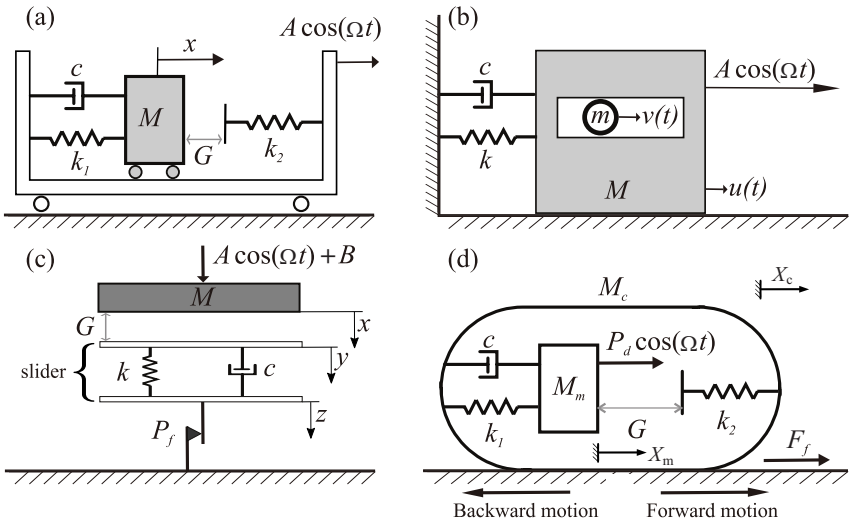

Figure 1: Typical vibro-impact systems: (a) the impact oscillator, (b) the vibro-impact nonlinear energy sink, (c) the drifting oscillator with unidirectional drift and (d) the vibro-impact capsule system with bidirectional drifts.

frequency-domain response for vibro-impact nonlinear energy sinks, which were verified both numerically and experimentally. For a 'bouncing ball' vibro-impact system, the conditions of stability, saddle-node and period-doubling bifurcations were analytically obtained in [22, 27]. In [11, 28, 29], semi-analytical methods were developed to reconstruct the system response, which can be used to calculate the system dynamics in an exact way without numerical integration. For a vibro-impact oscillator with bidirectional drifts, analytical conditions of the friction-induced stick-slip transitions were derived in [30]. Then such an analytical method was used to optimise the design in order to achieve the desired unidirectional drift at a high speed.

The present work has a specific focus on the vibro-impact capsule system with bidirectional drifts, which has shown potential applicability for medical diagnosis [9]. Compared to the other locomotion mechanisms described in [31], this vibro-impact system does not require external moving parts and has its own advantages for moving in the complex environments. This concept was inspired by the two-mass system in [32, 33] and the drifting oscillator in [11]. For such a non-smooth dynamical system involving impact and friction, its dynamics are sensitive to environmental friction [34–36], design parameters [12, 37] and driven force [38, 39]. There exists an optimum orbit of the system in terms of its progression speed and energy efficiency [9, 12, 39], of which the period-1 motion with one impact per period of external excitation [12, 39]. The impact event can significantly magnify the driven force of the system [8], especially when the environmental friction is relatively large. Therefore, detecting the onset conditions of the grazing and adding-sliding bifurcations for forward drifting is vital for system dynamics optimisation.

As will be seen from the equations of motion of the capsule system, the resulting model can be studied in the framework of piecewise-smooth dynamical systems [40], which are characterized by solution segments of smooth evolution interrupted by discrete events, such as switches, impacts, stick-slip transitions, etc. In general, the dynamical behaviour of such models is described in terms of their operation modes, which consist of a smooth vector field that governs the system evolution during the mode and rules that define the termination of the operation mode and possible transition to a next one. The terminal condition for an operation mode is usually given by the zero-set of smooth event functions, which are generally linked to the discrete events mentioned earlier (impacts, switches, etc.). This mathematical framework allows the implementation of specialized numerical techniques to carry out the numerical continuation and bifurcation detection of periodic solutions for piecewise-smooth dynamical systems, executed via software packages such as SlideCont [41], TC-HAT [42] and COCO [43]. In this work, the latter computational platform will be used to carry out a detailed numerical study of the capsule system, via the set of continuation routines provided by the COCO-toolbox 'hspo'.

On the other hand, since the dynamics of the capsule system is characterised as piecewise-smooth, the

trajectory of the system can be divided into six disjoint subregions, within which the system dynamics are all linear [44]. It is possible to solve the system orbit analytically in each subregion and then join them together to form a complete trajectory according to the switching mechanisms on the boundaries among these subregions. Compared to the aforementioned studies in [23–27, 30], the analytical solutions of the capsule system that involves impact and bidirectional drifts are more difficult to be derived. For the impact system with unidirectional drift [11, 28, 29], the analytical approach only considered one non-smoothness (i.e., either impact or friction). In addition, a vibration-driven two-mass system was analytically studied in [30] to derive the conditions for various stick-slip transitions. Different from those works, the capsule system in the present study is subjected to bidirectional drifts experiencing friction and impact simultaneously. The authors have studied this system in the past few years focusing on numerical modelling and analysis [12, 34, 36, 44, 45], control [10, 20, 38] and experimental verification [8, 9, 37, 39]. Different from these works, the contribution of the present paper is on the development of numerical and analytical approaches for detecting the onset conditions of the impact-induced grazing bifurcation and the friction-induced adding-sliding bifurcation for the capsule system. The present study is an extension work of Guo and Liu [44] but provides further insight into these two special bifurcations in the system.

The rest of this paper is organised as follows. Section 2 gives an overview of the mathematical modelling of the vibro-impact capsule system. Section 3 formulates the mathematical model further for path-following analysis. In Section 4, the analytical onset condition for grazing bifurcation and the semi-analytical onset condition for adding-sliding bifurcation are derived. Both the numerical and experimental results are discussed in Section 5. Finally, conclusions are drawn in Section 6.

2. Mathematical model of the capsule system

The two-degrees-of-freedom capsule system shown in Fig. 1(d) is considered in this work, where an inner mass M_m is connected to a rigid capsule M_c via a spring with stiffness k_1 and a damper with damping coefficient c. The inner mass is driven by a harmonic force $P_d\cos(\Omega t)$, where P_d, Ω and t represent the amplitude, frequency and time of the excitation, respectively. A secondary spring with stiffness k_2 is attached to the capsule, and the gap between the inner mass and the secondary spring is G. X_c and V_c represent the displacement and velocity of the capsule, whilst X_m and V_m represent the displacement and velocity of the inner mass, respectively. In this study, Coulomb friction is used to calculate the frictional force between the capsule and the supporting surface,

$$\begin{cases} F_f \in [-P_f,\, P_f], & V_c = 0, \\ F_f = -\text{sign}(V_c)P_f, & V_c \neq 0, \end{cases} \tag{1}$$

where $P_f = \mu(M_m + M_c)g$, μ is the friction coefficient between the capsule and the supporting surface, and g is the acceleration due to gravity.

The natural frequency of the capsule system is $\Omega_0 = \sqrt{\frac{k_1}{M_m}}$. Here, for simplicity, we introduce the following non-dimensional system parameters,

$$\tau = \Omega_0 t,\ \omega = \frac{\Omega}{\Omega_0},\ \alpha = \frac{P_d}{P_f},\ \zeta = \frac{c}{2M_m\Omega_0},\ \delta = \frac{k_1}{P_f}G,\ \beta = \frac{k_1}{k_2},\ \gamma = \frac{M_c}{M_m},\ f_b = \frac{max(|F_f|)}{P_f},$$

to represent the non-dimensional time, excitation frequency and amplitude, damping coefficient, gap, stiffness ratio, mass ratio and friction, respectively. Then the system variables can be converted to a non-dimensional form as follows

$$x_c = \frac{k_1}{P_f}X_c,\ v_c = \frac{\mathrm{d}x_c}{\mathrm{d}\tau} = \frac{k_1}{\Omega_0 P_f}X_c,\ \dot{v}_c = \frac{\mathrm{d}v_c}{\mathrm{d}\tau} = \frac{k_1}{\Omega_0^2 P_f}\ddot{X}_c,\ x_m = \frac{k_1}{P_f}X_m,$$

$$v_m = \frac{\mathrm{d}x_m}{\mathrm{d}\tau} = \frac{k_1}{\Omega_0 P_f}X_m,\ \dot{v}_m = \frac{\mathrm{d}v_m}{\mathrm{d}\tau} = \frac{k_1}{\Omega_0^2 P_f}\ddot{X}_m.$$

Therefore, the equations of motion for the capsule system can be written in a compact form as follows.

$$\begin{cases} \dot{x}_m &= v_m, \\ \dot{v}_m &= \alpha\cos(\omega\tau) - x_r - 2\zeta v_r - H_3\beta(x_r-\delta), \\ \dot{x}_c &= v_c, \\ \dot{v}_c &= \left(H_1(1-H_3)+H_2H_3\right)\left(-\text{sign}(v_c)f_b + x_r + 2\zeta v_r + H_3\beta(x_r-\delta)\right)/\gamma, \end{cases} \tag{2}$$

with $H_1 := H(|x_r + 2\zeta v_r| - f_b)$, $H_2 := H(|x_r + 2\zeta v_r + \beta(x_r-\delta)| - f_b)$, $H_3 := H(x_r-\delta)$, where $H(\cdot)$ stands for the Heaviside step function, while $x_r = x_m - x_c$ and $v_r = v_m - v_c$ are the relative displacement and velocity between the inner mass and the capsule, respectively. A detailed model derivation for the considered capsule system can be found in [12].

From a practical point of view, one of the main concerns in capsule applications is to investigate the influence of the system parameters on the average rate of progression (drift) per period of the capsule, which can be computed as follows

$$V_{\text{AVG}} := \frac{1}{T}\int_0^T v_c(\tau)\,d\tau, \tag{3}$$

whose sign indicates whether the capsule moves forward ($V_{\text{AVG}} > 0$) or backward ($V_{\text{AVG}} < 0$), and $T > 0$ is the period of the considered periodic solution. Due to the non-smoothness in impact and friction, the nonlinear dynamics of the capsule system are rich and complex. Consequently, the capsule's average rate of progression is critically sensitive to the system parameters. For the detailed study of parametric influence, readers can refer to [12]. The second solution measure used in the present study is related to the average power dissipated by the capsule system per period, defined as

$$P_{\text{AVG}} := \frac{1}{T}\int_0^T \alpha\cos(\omega\tau)v_m(\tau)\,d\tau. \tag{4}$$

With these two indicators it is possible to define optimal operations conditions for the capsule system, in terms of desired average velocity and power consumption, as will be seen later.

3. Mathematical formulation of the capsule model as a piecewise-smooth dynamical system

As mentioned in the introduction, the equations of motion of the capsule system (2) can be studied in the framework of piecewise-smooth dynamical systems [40], whose dynamical behaviour is described in terms of certain operation modes. Such modes are characterized by a smooth vector field that governs the system evolution during the mode and rules that define the termination of the operation mode and possible transition to a next one. This mathematical framework allows a numerical investigation of the system motion via path-following methods for piecewise-smooth dynamical systems, which will be implemented in the present work by means of the computational platform COCO [43]. To begin with, we will formulate the periodically forced model as an autonomous system using the standard nonlinear oscillator (cf. [46]):

$$\begin{cases} r' = r + \omega s - r\left(r^2+s^2\right), \\ s' = s - \omega r - s\left(r^2+s^2\right), \end{cases} \tag{5}$$

which has the asymptotically stable solution, $r(\tau) = \sin(\omega\tau)$ and $s(\tau) = \cos(\omega\tau)$, $\tau \geq 0$.

Let us denote by $u := (x_r, v_m, v_r, r, s)^T \in \mathbb{R}^5$ and $\lambda := (\omega, \alpha, \zeta, \delta, \beta, \gamma) \in \left(\mathbb{R}^+\right)^6$ the state variables and parameters of the system, respectively, with $\mathbb{R}^+$ being the set of positive numbers. Note that the state variables do not include a coordinate for the capsule displacement. However, we will see later on how to reconstruct the capsule position from the state variable u. In this way, we can consider a reduced form of the capsule model in order to improve the computational cost of the numerical analysis. Under

this preliminary mathematical framework, the operation modes to describe the capsule dynamics are given below.

No Contact - Stationary ($I_{NC\text{-}ST}$). This operation mode occurs when three conditions are met: the internal mass (M_m) and the secondary spring (k_2) are not in contact (see Fig. 1(d)), the force acting on the capsule via the internal mass support (k_1, c) does not exceed the threshold of the dry friction and the capsule velocity ($v_m - v_r$) is zero, that is

$$x_r < \delta, \quad |x_r + 2\zeta v_r| \leq 1 \ \text{ and } \ v_m - v_r = 0.$$

The motion of the capsule during this regime is governed by the equation (cf. (2) and (5))

$$u' = f_{\text{NC-ST}}(u, \lambda) := \begin{pmatrix} v_m \\ \alpha s - x_r - 2\zeta v_r \\ \alpha s - x_r - 2\zeta v_r \\ r + \omega s - r\left(r^2 + s^2\right) \\ s - \omega r - s\left(r^2 + s^2\right) \end{pmatrix}. \tag{6}$$

This operation mode can terminate in three different ways. The first one is when the internal mass hits the secondary spring, which occurs when the trajectory intersects transversally the discontinuity boundary

$$S_{\text{IMP}} := \left\{(x_r, v_m, v_r, r, s) \in \mathbb{R}^5 : x_r - \delta = 0\right\},$$

and the system then switches to the mode *Contact - Stationary* (defined below). The next terminal condition is given when the force acting on the capsule via the internal mass support becomes larger than 1, in which case the solution intersects transversally the discontinuity boundary

$$\ell_{\text{NC-FD}} := \left\{(x_r, v_m, v_r, r, s) \in \mathbb{R}^5 : x_r + 2\zeta v_r - 1 = 0 \ \text{ and } \ v_m - v_r = 0\right\}.$$

After the transversal intersection takes place, the system switches to the mode *No Contact - Forward Drift* defined below. Finally, the present operation mode can also terminate when the force acting on the capsule via the internal mass support becomes smaller than -1, which can be detected when the solution meets transversally the discontinuity boundary

$$\ell_{\text{NC-BD}} := \left\{(x_r, v_m, v_r, r, s) \in \mathbb{R}^5 : x_r + 2\zeta v_r + 1 = 0 \ \text{ and } \ v_m - v_r = 0\right\},$$

after which the system changes to the mode *No Contact - Backward Drift* to be defined later.

No Contact - Forward Drift ($I_{NC\text{-}FD}$). This mode is characterized by the conditions:

$$x_r < \delta \ \text{ and } \ v_m - v_r > 0,$$

i.e., the internal mass and the secondary spring are detached and the capsule moves forward. In this case, the dynamics of the system is described by (cf. (2) and (5))

$$u' = f_{\text{NC-FD}}(u, \lambda) := \begin{pmatrix} v_r \\ \alpha s - x_r - 2\zeta v_r \\ \alpha s - (x_r + 2\zeta v_r)\left(1 + \frac{1}{\gamma}\right) + \frac{1}{\gamma} \\ r + \omega s - r\left(r^2 + s^2\right) \\ s - \omega r - s\left(r^2 + s^2\right) \end{pmatrix}. \tag{7}$$

This operation regime can terminate in two ways: when the internal mass hits the secondary spring and when the capsule velocity ($v_m - v_r$) becomes zero. The first case, as before, is detected when the trajectory crosses the boundary S_{IMP} defined above, after which the system changes to the mode *Contact*

- *Forward Drift* (see below). In the second case, the trajectory meets the discontinuity boundary

$$S_{\text{VC0}} := \left\{ (x_r, v_m, v_r, r, s) \in \mathbb{R}^5 : v_m - v_r = 0 \right\}.$$

After this event occurs, the next operation mode depends on the force acting on the capsule via the internal mass support $(x_r + 2\zeta v_r)$. Specifically, if $|x_r + 2\zeta v_r| \leq 1$ then the system switches to the mode *No Contact - Stationary*, where the capsule velocity is zero. On the other hand, if $x_r + 2\zeta v_r < -1$, the next operation mode is *No Contact - Backward Drift*.

No Contact - Backward Drift ($I_{NC\text{-}BD}$). This operation mode is analogous to the one above, except that now the capsule moves backward, that is

$$x_r < \delta \quad \text{and} \quad v_m - v_r < 0.$$

The dynamics of the capsule is described by the system of ODEs (cf. (2) and (5))

$$u' = f_{\text{NC-BD}}(u, \lambda) := \begin{pmatrix} v_r \\ \alpha s - x_r - 2\zeta v_r \\ \alpha s - (x_r + 2\zeta v_r)\left(1 + \frac{1}{\gamma}\right) - \frac{1}{\gamma} \\ r + \omega s - r\left(r^2 + s^2\right) \\ s - \omega r - s\left(r^2 + s^2\right) \end{pmatrix}. \tag{8}$$

Similarly to the previous case, this operation regime finishes when the internal mass hits the secondary spring (i.e. the trajectory crosses the boundary S_{IMP}) or when the capsule velocity becomes zero (intersection with S_{VC0}). In the first case, the system switches to the mode *Contact - Backward Drift* to be defined below. If the capsule velocity becomes zero, the next segment is determined in a similar way as before. If $|x_r + 2\zeta v_r| \leq 1$, then the system switches to the mode *No Contact - Stationary*, and if $x_r + 2\zeta v_r > 1$, the next operation mode is *No Contact - forward Drift*.

Contact - Stationary ($I_{C\text{-}ST}$). This operation regime is analogous to the *No Contact - Stationary* mode. The difference is that now the internal mass is in contact with the secondary spring, hence an additional term has to be considered in the restoring force, and therefore the conditions for this mode are:

$$x_r \geq \delta, \quad \left| x_r + 2\zeta v_r + \beta(x_r - \delta) \right| \leq 1 \quad \text{and} \quad v_m - v_r = 0.$$

The motion of the capsule is governed in this case by the system (cf. (2) and (5))

$$u' = f_{\text{C-ST}}(u, \lambda) := \begin{pmatrix} v_m \\ \alpha s - x_r - 2\zeta v_r - \beta(x_r - \delta) \\ \alpha s - x_r - 2\zeta v_r - \beta(x_r - \delta) \\ r + \omega s - r\left(r^2 + s^2\right) \\ s - \omega r - s\left(r^2 + s^2\right) \end{pmatrix}. \tag{9}$$

The terminal conditions for this regime are also analogous to those defined for the *No Contact - Stationary* mode. In this case, a transversal intersection with the following boundaries is monitored: S_{IMP} and

$$\ell_{\text{C-FD}} := \left\{ (x_r, v_m, v_r, r, s) \in \mathbb{R}^5 : x_r + 2\zeta v_r + \beta(x_r - \delta) - 1 = 0 \quad \text{and} \quad v_m - v_r = 0 \right\},$$

$$\ell_{\text{C-BD}} := \left\{ (x_r, v_m, v_r, r, s) \in \mathbb{R}^5 : x_r + 2\zeta v_r + \beta(x_r - \delta) + 1 = 0 \quad \text{and} \quad v_m - v_r = 0 \right\}.$$

In this mode, a transversal intersection with the boundary S_{IMP} means the contact between the mass and the secondary spring is lost, hence the system moves to the *No Contact - Stationary* mode. On the other hand, if the solution meets transversally the boundary $\ell_{\text{C-FD}}$, then the force acting on the capsule from the mass becomes larger than 1, and therefore the capsule starts moving forward and the system changes to the mode *Contact - Forward Drift* defined later. Lastly, if the trajectory crosses the boundary $\ell_{\text{C-BD}}$,

it means that the force acting on the capsule from the mass becomes smaller than -1, due to which the capsule begins to move backward. In this case, the next operation mode is *Contact - Backward Drift* to be defined at the end.

Contact - Forward Drift ($I_{C\text{-}FD}$). This operation regime is characterized by the conditions:

$$x_r \geq \delta \quad \text{and} \quad v_m - v_r > 0,$$

analogously to the *No Contact - Forward Drift* mode. The capsule dynamics is described by the equation (cf. (2) and (5))

$$u' = f_{\text{C-FD}}(u,\lambda) := \begin{pmatrix} v_r \\ \alpha s - x_r - 2\zeta v_r - \beta(x_r - \delta) \\ \alpha s - \left(x_r\left(\beta+1\right) + 2\zeta v_r\right)\left(1+\frac{1}{\gamma}\right) + \frac{1}{\gamma}\left(\beta\delta(1+\gamma)+1\right) \\ r + \omega s - r\left(r^2+s^2\right) \\ s - \omega r - s\left(r^2+s^2\right) \end{pmatrix}. \tag{10}$$

As with the *No Contact - Forward Drift* mode, this operation regime can finish in two ways. The first one occurs when the trajectory intersects transversally the boundary S_{IMP}, meaning that the contact between the internal mass and the secondary spring is lost, and therefore the capsule switches to the *No Contact - Forward Drift* regime. In the second case the solution meets the discontinuity boundary S_{VC0} defined previously, which implies that the capsule velocity becomes zero. As before, the next operation mode depends on the force acting on the capsule from the mass ($x_r + 2\zeta v_r + \beta(x_r - \delta)$). That is, if $\left|x_r + 2\zeta v_r + \beta(x_r - \delta)\right| \leq 1$ then the system switches to the mode *Contact - Stationary*, while if $x_r + 2\zeta v_r + \beta(x_r - \delta) < -1$, the next operation mode is *Contact - Backward Drift* (see below).

Contact - Backward Drift ($I_{C\text{-}BD}$). This operation mode is similar to the *No Contact - Backward Drift* case. As before, the conditions characterizing this regime are given by

$$x_r \geq \delta \quad \text{and} \quad v_m - v_r < 0.$$

The motion of the capsule is described in this case by the system of ODEs (cf. (2) and (5))

$$u' = f_{\text{C-BD}}(u,\lambda) := \begin{pmatrix} v_r \\ \alpha s - x_r - 2\zeta v_r - \beta(x_r - \delta) \\ \alpha s - \left(x_r\left(\beta+1\right) + 2\zeta v_r\right)\left(1+\frac{1}{\gamma}\right) + \frac{1}{\gamma}\left(\beta\delta(1+\gamma)-1\right) \\ r + \omega s - r\left(r^2+s^2\right) \\ s - \omega r - s\left(r^2+s^2\right) \end{pmatrix}. \tag{11}$$

This mode of operation can also terminate in two ways as in the previous cases: when the internal mass loses contact with the secondary spring (i.e. the trajectory crosses the boundary S_{IMP}) or when the capsule velocity becomes zero (intersection with S_{VC0}). In the first situation, the system switches to the mode *No Contact - Backward Drift*. If the capsule velocity becomes zero, the next segment depends again on the force acting on the capsule from the mass (see previous modes). If $\left|x_r + 2\zeta v_r + \beta(x_r - \delta)\right| \leq 1$, then the system switches to the mode *Contact - Stationary*, and if $x_r + 2\zeta v_r + \beta(x_r - \delta) > 1$, the next operation mode is *Contact - forward Drift*.

Finally, the capsule model can be formulated in terms of the mathematical framework introduced before as follows:

No contact ($x_r < \delta$):

$$u' = \begin{cases} f_{\text{NC-ST}}(u,\lambda), & v_m - v_r = 0 \ \text{ and } \ |x_r + 2\zeta v_r| \leq 1, \\ f_{\text{NC-FD}}(u,\lambda), & v_m - v_r > 0 \ \text{ or } \ (v_m - v_r = 0 \ \text{ and } \ x_r + 2\zeta v_r > 1), \\ f_{\text{NC-BD}}(u,\lambda), & v_m - v_r < 0 \ \text{ or } \ (v_m - v_r = 0 \ \text{ and } \ x_r + 2\zeta v_r < -1). \end{cases} \tag{12}$$

Contact ($x_r \geq \delta$):

$$u' = \begin{cases} f_{\text{C-ST}}(u,\lambda), & v_m - v_r = 0 \ \text{ and } \ \left|x_r + 2\zeta v_r + \beta(x_r - \delta)\right| \leq 1, \\ f_{\text{C-FD}}(u,\lambda), & v_m - v_r > 0 \ \text{ or } \ \left(v_m - v_r = 0 \ \text{ and } \ x_r + 2\zeta v_r + \beta(x_r - \delta) > 1\right), \\ f_{\text{C-BD}}(u,\lambda), & v_m - v_r < 0 \ \text{ or } \ \left(v_m - v_r = 0 \ \text{ and } \ x_r + 2\zeta v_r + \beta(x_r - \delta) < -1\right). \end{cases} \tag{13}$$

As mentioned earlier, note that the state variables in this formulation do not include a coordinate for the capsule position. This information, however, can be recovered from model (12)–(13) as follows:

$$x_c(\tau) = x_c^* + \int_0^\tau (v_m(s) - v_r(s))\, ds,$$

where $x_c^* \in \mathbb{R}$ represents the position of the capsule at $\tau = 0$. A typical periodic response of the proposed model can be found in Fig. 2, showing all the operation modes described in this section.

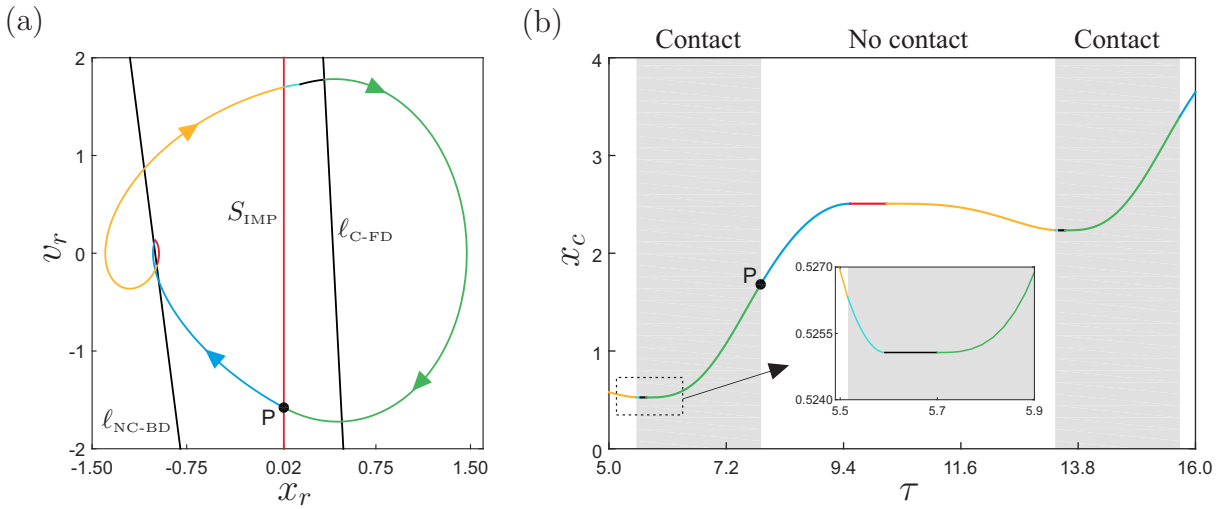

Figure 2: Periodic solution of the capsule model (12)–(13) computed for the parameter values $\omega = 0.8$, $\alpha = 1.49$, $\zeta = 0.05$, $\delta = 0.02$, $\beta = 1.5$ and $\gamma = 3.3$. Panel (a) shows a phase plot with the following operation modes starting from the reference point P (clockwise): $I_{\text{NC-FD}}$ (*No Contact - Forward Drift*, blue), $I_{\text{NC-ST}}$ (*No Contact - Stationary*, red), $I_{\text{NC-BD}}$ (*No Contact - Backward Drift*, yellow), $I_{\text{C-BD}}$ (*Contact - Backward Drift*, light blue), $I_{\text{C-ST}}$ (*Contact - Stationary*, black) and $I_{\text{C-FD}}$ (*Contact - Forward Drift*, green). The panel also depicts the discontinuity boundaries $\ell_{\text{NC-BD}}$, $\ell_{\text{C-FD}}$ and S_{IMP}, defined in Section 3. Panel (b) presents the corresponding time plot showing the capsule position, using the color code as in panel (a). Grey areas represent the contact modes.

4. Analytical onset conditions of grazing and adding-sliding bifurcations

As described in Section 3, the nonlinear mathematical model in Eq. (2) can be divided into six operation modes, each of which described by a linear ODE. According to [44], the trajectory of the capsule system in 3-dimensional space can be expressed in subspaces divided by non-smooth boundary surfaces and lines as visualised in Fig. 3. Since the present study concerns the discontinuity-induced bifurcations in the capsule system, the semi-analytic solutions of the operation modes, $I_{\text{NC-ST}}$ and $I_{\text{C-ST}}$, will be derived in this section. These two operation modes correspond to the occurrence of the grazing and the adding-sliding bifurcations induced by the discontinuities of impact and dry friction in the system, respectively. A top view of the $v_c = 0$ plane in Fig. 3 is shown in Fig. 4, with the red and black segments representing the system dynamics governed by $I_{\text{NC-ST}}$ and $I_{\text{C-ST}}$, respectively. In Fig. 4(a), the orbit stays in the $I_{\text{NC-ST}}$ region, i.e. the light-blue shadowed area enveloped by the boundary lines $L_1 := x_r + 2\zeta v_r = -f_b$, $L_1' := x_r + 2\zeta v_r = f_b$ and $L_2 := x_r = \delta$. A grazing bifurcation occurs in Fig. 4(b) where the orbit grazes the impact boundary L_2 at the point P_0. In Fig. 4(c), the orbit has two segments,

$I_{\text{NC-ST}}$ (in red) and $I_{\text{C-ST}}$ (in black). The $I_{\text{C-ST}}$ region is the grey shadowed area enveloped by the boundary lines L_2, $L_3 := x_r + 2\zeta v_r + \beta(x_r - \delta) = f_b$ and $L_3^{'} := x_r + 2\zeta v_r + \beta(x_r - \delta) = -f_b$. An adding-sliding bifurcation occurs in Fig. 4(d) where the orbit grazes the boundary line L_3 at the point P_2. Next we will derive the analytical solutions for all the four cases shown in Fig. 4.

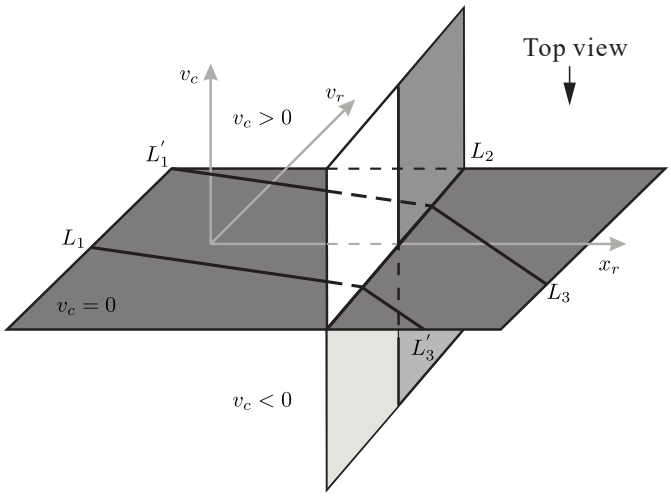

Figure 3: Subspaces, non-smooth boundary surfaces and lines for the capsule system in 3-dimensional space, where $L_1 := x_r + 2\zeta v_r = -f_b$, $L_1^{'} := x_r + 2\zeta v_r = f_b$, $L_2 := x_r = \delta$, $L_3 := x_r + 2\zeta v_r + \beta(x_r - \delta) = f_b$ and $L_3^{'} := x_r + 2\zeta v_r + \beta(x_r - \delta) = -f_b$.

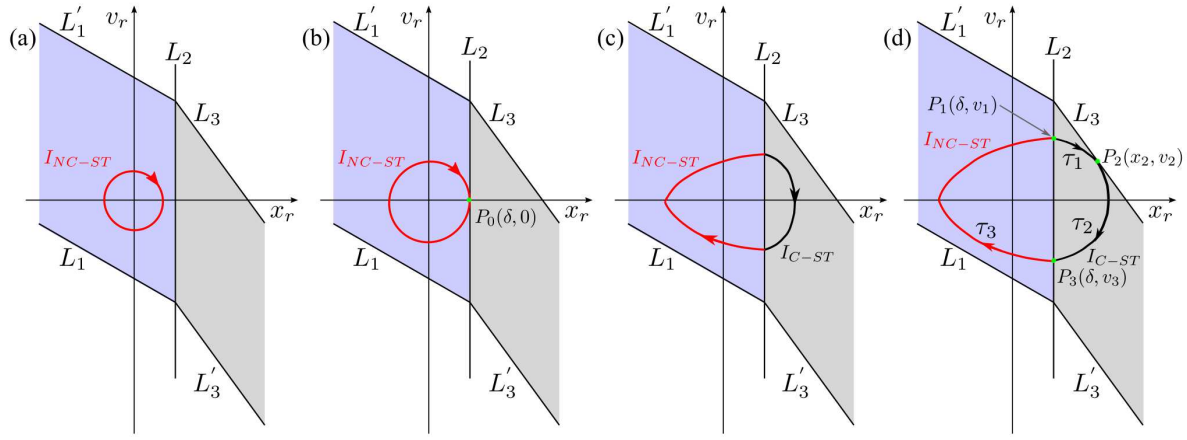

Figure 4: Orbits on the $v_c = 0$ plane from the top view of Fig. 3. (a) The orbit stays in the $I_{\text{NC-ST}}$ region, the light-blue shadowed area enveloped by the boundaries $L_1 := x_r + 2\zeta v_r = -f_b$, $L_1^{'} := x_r + 2\zeta v_r = f_b$ and $L_2 := x_r = \delta$. (b) A grazing bifurcation occurs and the orbit grazes the impact boundary L_2 at the point $P_0(\delta, 0)$. (c) The orbit consists of the $I_{\text{NC-ST}}$ segment in red and the $I_{\text{C-ST}}$ segment in black. The $I_{\text{C-ST}}$ region is the grey shadowed area enveloped by the boundaries L_2, $L_3 := x_r + 2\zeta v_r + \beta(x_r - \delta) = f_b$ and $L_3^{'} := x_r + 2\zeta v_r + \beta(x_r - \delta) = -f_b$. (d) An adding-sliding bifurcation occurs, where the orbit grazes the boundary L_3 at the point $P_2(x_2, v_2)$, while the orbit intersects with the impact boundary L_2 at the points $P_1(\delta, v_1)$ and $P_3(\delta, v_3)$. The time intervals of $P_1 \mapsto P_2$, $P_2 \mapsto P_3$, and $P_3 \mapsto P_1$ are represented by τ_1, τ_2 and τ_3, respectively.

4.1. Analytical solution of the $I_{NC\text{-}ST}$ mode

For the $I_{\text{NC-ST}}$ mode, we have $v_c = 0$, $x_r \le \delta$ and $|x_r + 2\zeta v_r| \le f_b$. Then the relative displacement of the capsule system can be rewritten as

$$\ddot{x}_r + 2\zeta\dot{x}_r + x_r = \alpha\cos(\omega\tau + \phi_0), \tag{14}$$

where ϕ_0 represents the initial phase angle of the driven force. This is a second order linear nonhomogeneous differential equation with constant coefficients, and its corresponding characteristic equation can be written as

$$p^2 + 2\zeta_1\omega_{n1}p + \omega_{n1}^2 = 0, \tag{15}$$

where $\omega_{n1} = 1$ and $\zeta_1 = \frac{\zeta}{\omega_{n1}}$. Since its characteristic roots are $p_{1,2} = \lambda_1 + j\omega_{d1}$, where $\lambda_1 = -\zeta_1\omega_{n1}$ and $\omega_{d1} = \omega_{n1}\sqrt{1-\zeta_1^2}$, Eq. (14) can be rewritten as

$$\ddot{x}_r + 2\zeta_1\omega_{n1}\dot{x}_r + \omega_{n1}^2 x_r = \alpha\cos(\omega\tau + \phi_0). \tag{16}$$

A particular solution of Eq. (16) can be written as

$$x_{r1} = A_1\cos(\omega\tau + \phi_0) + B_1\sin(\omega\tau + \phi_0), \tag{17}$$

where $A_1 = \frac{\alpha(\omega_{n1}^2-\omega^2)}{(\omega_{n1}^2-\omega^2)^2+(2\zeta_1\omega_{n1}\omega)^2}$ and $B_1 = \frac{\alpha(2\zeta_1\omega_{n1}\omega)}{(\omega_{n1}^2-\omega^2)^2+(2\zeta_1\omega_{n1}\omega)^2}$ are constant coefficients.

Since the related homogeneous equation of Eq. (14) can be rewritten as

$$\ddot{x}_r + 2\zeta_1\omega_{n1}\dot{x}_r + \omega_{n1}^2 x_r = 0, \tag{18}$$

its general solution can be obtained as

$$x_{r2} = D_1 e^{\lambda_1\tau}\cos(\omega_{d1}\tau) + E_1 e^{\lambda_1\tau}\sin(\omega_{d1}\tau), \tag{19}$$

where D_1 and E_1 are unknown constant coefficients, but can be determined by the initial conditions of the system.

Based on the superposition principle, the analytical solution of Eq. (14) is the sum of the particular solution of the nonhomogeneous equation in Eq. (14), x_{r1}, and the general solution of the homogeneous equation in Eq. (18), x_{r1}, given as

$$x_r = x_{r1} + x_{r2} = A_1\cos(\omega\tau + \phi_0) + B_1\sin(\omega\tau + \phi_0) + D_1 e^{\lambda_1\tau}\cos(\omega_{d1}\tau) + E_1 e^{\lambda_1\tau}\sin(\omega_{d1}\tau). \tag{20}$$

Consequently, the analytical solution of the relative velocity, $v_r = \dot{x}_r$, is given as

$$v_r = B_1\omega\cos(\omega\tau + \phi_0) - A_1\omega\sin(\omega\tau + \phi_0) + F_1 e^{\lambda_1\tau}\cos(\omega_{d1}\tau) + G_1 e^{\lambda_1\tau}\sin(\omega_{d1}\tau). \tag{21}$$

where $F_1 = D_1\lambda_1 + E_1\omega_{d1}$ and $G_1 = E_1\lambda_1 - D_1\omega_{d1}$.

Without the loss of generality, the initial conditions are defined as x_{r0}, v_{r0} and ϕ_0, representing the initial relative displacement and velocity, and the initial phase angle of the driven force, respectively. The initial time can be set as $\tau_0 = 0$. Substituting these initial conditions into Eqs. (20) and (21) gives

$$x_{r0} = A_1\cos(\phi_0) + B_1\sin(\phi_0) + D_1, \tag{22}$$

$$v_{r0} = B_1\omega\cos(\phi_0) - A_1\omega\sin(\phi_0) + D_1\lambda_1 + E_1\omega_{d1}. \tag{23}$$

Solving Eqs. (22) and (23) gives the analytical expressions of $D_1 = x_{r0} - A_1\cos(\phi_0) - B_1\sin(\phi_0)$ and $E_1 = [v_{r0} - D_1\lambda_1 - B_1\omega\cos(\phi_0) + A_1\omega\sin(\phi_0)]/\omega_{d1}$.

In summary, the analytical solution of the $I_{\text{NC-ST}}$ mode expressed in Eq. (14) can be obtained using

$$x_r = A_1\cos(\omega\tau + \phi_0) + B_1\sin(\omega\tau + \phi_0) + J_1 e^{\lambda_1\tau}\cos(\omega_{d1}\tau) + K_1 e^{\lambda_1\tau}\sin(\omega_{d1}\tau), \tag{24}$$

$$v_r = B_1\omega\cos(\omega\tau + \phi_0) - A_1\omega\sin(\omega\tau + \phi_0) + F_1 e^{\lambda_1\tau}\cos(\omega_{d1}\tau) + G_1 e^{\lambda_1\tau}\sin(\omega_{d1}\tau), \tag{25}$$

where $J_1 = D_1$ and $K_1 = E_1$.

4.2. Analytical onset condition of grazing bifurcation

As shown in Fig. 4(b), a grazing bifurcation occurs when the orbit grazes the impact boundary L_2 at the point $P_0(\delta, 0)$. For this grazing bifurcation, only the steady-state response is considered. The

analytical solution of the $I_{\text{NC-ST}}$ mode in Eq. (24) consists of two parts, including the steady-state solution x_{r1} in Eq. (17) and the transient solution x_{r2} in Eq. (19). Since $\lambda_1 = -\zeta_1\omega_{n1} < 0$, $x_{r1} \to 0$ as $\tau \to \infty$. So when the grazing bifurcation occurs, $\max(x_{r1}) = \delta$ holds, such that

$$A_1^2 + B_1^2 = \delta^2, \tag{26}$$

that is

$$\alpha^2 = \delta^2[(\omega_{n1}^2 - \omega^2)^2 + (2\zeta_1\omega_{n1}\omega)^2]. \tag{27}$$

As $\alpha \geq 0$, $\delta \geq 0$, $\omega_{n1} = 1$ and $\zeta_1 = \zeta$, the analytical onset condition of the grazing bifurcation can be simplified as

$$\alpha = \delta\sqrt{(1-\omega^2)^2 + (2\zeta\omega)^2}. \tag{28}$$

The analytical onset condition of the grazing bifurcation in Eq. (28) only depends on the system parameters ζ and δ, and the control parameters α and ω, while is independent of its initial conditions (i.e., x_{r0}, v_{r0}, τ_0 and ϕ_0) and the system parameters β and γ. In practical applications, e.g. the capsule endoscopy [39], this grazing condition has significance on optimising capsule's trajectory. Related results are shown and discussed in Section 5.3.

4.3. Analytical solution of the $I_{C\text{-}ST}$ mode

For the $I_{\text{C-ST}}$ mode presented in Fig. 4(c), the grey-shadowed region satisfies $v_c = 0$, $x_r \geq \delta$ and $|x_r + 2\zeta v_r + \beta(x_r - \delta)| \leq f_b$. Then the relative motion of the capsule system can be written as

$$\ddot{x}_r + 2\zeta\dot{x}_r + (1+\beta)x_r = \alpha\cos(\omega\tau + \phi_0) + \beta\delta. \tag{29}$$

The corresponding characteristic equation of Eq. (29) is

$$p^2 + 2\zeta_2\omega_{n2}p + \omega_{n2}^2 = 0, \tag{30}$$

where $\omega_{n2} = \sqrt{1+\beta}$ and $\zeta_2 = \frac{\zeta}{\omega_{n2}}$. Here, its characteristic roots are $p_{1,2} = \lambda_2 + j\omega_{d2}$, where $\lambda_2 = -\zeta_2\omega_{n2}$ and $\omega_{d2} = \omega_{n2}\sqrt{1-\zeta_2^2}$.

Therefore, one nonhomogeneous equation of Eq. (29) can be written as

$$\ddot{x}_r + 2\zeta_2\omega_{n2}\dot{x}_r + \omega_{n2}^2 x_r = \alpha\cos(\omega\tau + \phi_0), \tag{31}$$

with a particular solution given as

$$x_{r1} = A_2\cos(\omega\tau + \phi_0) + B_2\sin(\omega\tau + \phi_0), \tag{32}$$

where $A_2 = \frac{\alpha(\omega_{n2}^2 - \omega^2)}{(\omega_{n2}^2 - \omega^2)^2 + (2\zeta_2\omega_{n2}\omega)^2}$ and $B_2 = \frac{\alpha(2\zeta_2\omega_{n2}\omega)}{(\omega_{n2}^2 - \omega^2)^2 + (2\zeta_2\omega_{n2}\omega)^2}$ are constant coefficients. The other nonhomogeneous equation of Eq. (29) can be written as

$$\ddot{x}_r + 2\zeta_2\omega_{n2}\dot{x}_r + \omega_{n2}^2 x_r = \omega_{n2}^2 u_2, \tag{33}$$

with the particular solution

$$x_{r2} = -u_2 e^{\lambda_2\tau}\cos(\omega_{d2}\tau) - u_2 C_2 e^{\lambda_2\tau}\sin(\omega_{d2}\tau) + u_2, \tag{34}$$

where $u_2 = \frac{\beta\delta}{\omega_{n2}^2}$ and $C_2 = \frac{\zeta_2}{\sqrt{1-\zeta_2^2}}$.

On the other hand, the homogeneous equation about Eq. (29) can be obtained as

$$\ddot{x}_r + 2\zeta\dot{x}_r + (1+\beta)x_r = 0, \tag{35}$$

with its general solution given as

$$x_{r3} = D_2 e^{\lambda_2\tau}\cos(\omega_{d2}\tau) + E_2 e^{\lambda_2\tau}\sin(\omega_{d2}\tau), \tag{36}$$

where D_2 and E_2 are unknown constant coefficients, but can be determined by the initial conditions of the system.

Based on the superposition principle, the analytical solution of Eq. (14) is the sum of the particular solutions x_{r1} and x_{r2} and the general solution x_{r3} given as

$$\begin{aligned} x_r &= x_{r1} + x_{r2} + x_{r3} \\ &= A_2\cos(\omega\tau+\phi_0) + B_2\sin(\omega\tau+\phi_0) + (D_2-u_2)e^{\lambda_2\tau}\cos(\omega_{d2}\tau) \\ &\quad +(E_2-u_2C_2)e^{\lambda_2\tau}\sin(\omega_{d2}\tau) + u_2. \end{aligned} \tag{37}$$

Then the analytical solution of the relative velocity is

$$v_r = B_2\omega\cos(\omega\tau+\phi_0) - A_2\omega\sin(\omega\tau+\phi_0) + F_2e^{\lambda_2\tau}\cos(\omega_{d2}\tau) + G_2e^{\lambda_2\tau}\sin(\omega_{d2}\tau). \tag{38}$$

where $F_2 = (D_2-u_2)\lambda_2 + (E_2-u_2C_2)\omega_{d2}$ and $G_2 = (E_2-u_2C_2)\lambda_2 - (D_2-u_2)\omega_{d2}$.

If the initial conditions are known, Eqs. (37) and (38) can be rewritten as

$$x_{r0} = A_2\cos(\phi_0) + B_2\sin(\phi_0) + D_2 - u_2 + u_2, \tag{39}$$

$$v_{r0} = B_2\omega\cos(\phi_0) - A_2\omega\sin(\phi_0) + (D_2-u_2)\lambda_2 + (E_2-u_2C_2)\omega_{d2}. \tag{40}$$

By solving Eqs. (39) and (40), it gives $D_2 = x_{r0} - A_2\cos(\phi_0) - B_2\sin(\phi_0)$ and $E_2 = \frac{1}{\omega_{d2}}[v_{r0} - D_2\lambda_2 + u_2\lambda_2 - B_2\omega\cos(\phi_0) + A_2\omega\sin(\phi_0) + u_2C_2\omega_{d2}]$. Finally, the complete analytical solution for Eq. (29) is given as

$$x_r = A_2\cos(\omega\tau+\phi_0) + B_2\sin(\omega\tau+\phi_0) + J_2e^{\lambda_2\tau}\cos(\omega_{d2}\tau) + K_2e^{\lambda_2\tau}\sin(\omega_{d2}\tau) + u_2, \tag{41}$$

$$v_r = B_2\omega\cos(\omega\tau+\phi_0) - A_2\omega\sin(\omega\tau+\phi_0) + F_2e^{\lambda_2\tau}\cos(\omega_{d2}\tau) + G_2e^{\lambda_2\tau}\sin(\omega_{d2}\tau), \tag{42}$$

where $J_2 = D_2 - u_2$ and $K_2 = E_2 - u_2C_2$.

4.4. Semi-analytical onset condition of adding-sliding bifurcation

As shown in Fig. 4(d), the adding-sliding bifurcation occurs when the orbit grazes the boundary L_3 at the point $P_2(x_2, v_2)$. At this critical point, an infinitely small increase in α will lead to a forward motion of the capsule. As can be seen from the figure, the point $P_1(\delta, v_1)$ was chosen as the origin of the orbit with the initial time $\tau_0 = 0$ and the initial phase angle ϕ_1. The first segment $P_1(\delta, v_1) \mapsto P_2(x_2, v_2)$ is governed by the $I_{\text{C-ST}}$ mode within the time interval τ_1, which can be expressed by using the analytical solution in Eqs. (41) and (42). Hence, we have

$$x_2 = A_2\cos(\omega\tau+\phi_1) + B_2\sin(\omega\tau+\phi_1) + J_{21}e^{\lambda_2\tau}\cos(\omega_{d2}\tau) + K_{21}e^{\lambda_2\tau}\sin(\omega_{d2}\tau) + u_2, \tag{43}$$

$$v_2 = B_2\omega\cos(\omega\tau+\phi_1) - A_2\omega\sin(\omega\tau+\phi_1) + F_{21}e^{\lambda_2\tau}\cos(\omega_{d2}\tau) + G_{21}e^{\lambda_2\tau}\sin(\omega_{d2}\tau), \tag{44}$$

$$\phi_2 = \omega\tau_1 + \phi_1, \tag{45}$$

where A_2, B_2, C_2, u_2, λ_2 and ω_{d2} are constant coefficients given in Section 4.3, while the other coefficients can be obtained according to the initial conditions $x_{r0} = \delta$, $v_{r0} = v_1$ and $\phi_0 = \phi_0$ as

$$\begin{aligned} D_{21} &= \delta - A_2\cos(\phi_1) - B_2\sin(\phi_1), \\ E_{21} &= \tfrac{1}{\omega_{d2}}[v_1 + (u_2 - D_{21})\lambda_2 - B_2\omega\cos(\phi_1) + A_2\omega\sin(\phi_1) + u_2C_2\omega_{d2}], \\ J_{21} &= D_{21} - u_2, \\ K_{21} &= E_{21} - u_2C_2, \\ F_{21} &= (D_{21}-u_2)\lambda_2 + (E_{21}-u_2C_2)\omega_{d2}, \\ G_{21} &= (E_{21}-u_2C_2)\lambda_2 - (D_{21}-u_2)\omega_{d2}. \end{aligned}$$

Since the point $P_2(x_2, v_2)$ is on the boundary L_3, we have

$$x_2 + 2\zeta v_2 + \beta(x_2 - \delta) = f_b. \tag{46}$$

According to the orbit switching mechanism on the boundary [44], the vector field $P_2(x_2, v_2)$ is perpendicular to the normal vector L_3, so

$$(1+\beta)v_2 + 2\zeta[-x_2 - 2\zeta v_2 - \beta(x_2 - \delta)] = 0. \tag{47}$$

For the second segment $P_2(x_2, v_2) \mapsto P_3(\delta, v_3)$, the orbit is governed by the $I_{\text{C-ST}}$ mode within the time interval τ_2. Similar to the first segment, here we have

$$\begin{aligned}
\delta &= A_2\cos(\omega\tau+\phi_1) + B_2\sin(\omega\tau+\phi_1) + J_{22}e^{\lambda_2\tau}\cos(\omega_{d2}\tau) + K_{22}e^{\lambda_2\tau}\sin(\omega_{d2}\tau) + u_2, &(48)\\
v_3 &= B_2\omega\cos(\omega\tau+\phi_1) - A_2\omega\sin(\omega\tau+\phi_1) + F_{22}e^{\lambda_2\tau}\cos(\omega_{d2}\tau) + G_{22}e^{\lambda_2\tau}\sin(\omega_{d2}\tau), &(49)\\
\phi_3 &= \omega\tau_2 + \phi_2. &(50)
\end{aligned}$$

If the initial conditions for this segment are $x_{r0} = x_2$, $v_{r0} = v_2$ and $\phi_0 = \phi_2$, the coefficients can be calculated as

$$\begin{aligned}
D_{22} &= x_2 - A_2\cos(\phi_2) - B_2\sin(\phi_2),\\
E_{22} &= \tfrac{1}{\omega_{d2}}[v_2 + (u_2 - D_{22})\lambda_2 - B_2\omega\cos(\phi_2) + A_2\omega\sin(\phi_2) + u_2C_2\omega_{d2}],\\
J_{22} &= D_{22} - u_2,\\
K_{22} &= E_{22} - u_2C_2,\\
F_{22} &= (D_{22} - u_2)\lambda_2 + (E_{22} - u_2C_2)\omega_{d2},\\
G_{22} &= (E_{22} - u_2C_2)\lambda_2 - (D_{22} - u_2)\omega_{d2}.
\end{aligned}$$

For the third segment $P_3(\delta, v_3) \mapsto P_1(\delta, v_1)$, the orbit of the system is governed by the $I_{\text{NC-ST}}$ mode within the time interval τ_3. Then this segment can be expressed by using the analytical solution in Eqs. (24) and (25).

Finally, the three segments form a complete orbit of period-one motion as

$$\begin{aligned}
\delta &= A_1\cos(\omega\tau+\phi_3) + B_1\sin(\omega\tau+\phi_3) + J_{11}e^{\lambda_1\tau}\cos(\omega_{d1}\tau) + K_{11}e^{\lambda_1\tau}\sin(\omega_{d1}\tau), &(51)\\
v_1 &= B_1\omega\cos(\omega\tau+\phi_3) - A_1\omega\sin(\omega\tau+\phi_3) + F_{11}e^{\lambda_1\tau}\cos(\omega_{d1}\tau) + G_{11}e^{\lambda_1\tau}\sin(\omega_{d1}\tau), &(52)\\
T &= \tau_1 + \tau_2 + \tau_3, &(53)
\end{aligned}$$

where A_1, B_1, C_1, λ_1 and ω_{d1} are constant coefficients given in Section 4.1, and the other coefficients can be calculated by using the initial conditions $x_{r0} = \delta$, $v_{r0} = v_3$ and $\phi_0 = \phi_3$ as

$$\begin{aligned}
J_{11} &= D_{11} = \delta - A_1\cos(\phi_3) - B_1\sin(\phi_3),\\
K_{11} &= E_{11} = \tfrac{1}{\omega_{d1}}[v_3 - D_{11}\lambda_1 - B_1\omega\cos(\phi_3) + A_1\omega\sin(\phi_3)],\\
F_{11} &= D_{11}\lambda_1 + E_{11}\omega_{d1},\\
G_{11} &= E_{11}\lambda_1 - D_{11}\omega_{d1}.
\end{aligned}$$

In summary, to derive the analytical solutions of the $I_{\text{NC-ST}}$ and $I_{\text{C-ST}}$ modes, there are 11 equations in Eqs. (43)-(53) and 10 unknown variables, v_1, ϕ_1, τ_1, x_2, v_2, ϕ_2, τ_2, v_3, ϕ_3 and τ_3 to be determined. To detect the onset condition of the adding-sliding bifurcation, we can select one parameter from the system parameters ζ, δ, β and γ, or the control parameters α and ω, as the 11^{th} unknown variable for these 11 equations. For a specific capsule system, its system parameters are all fixed during operation, while its control parameters can be adjusted in real time. Thus, the parameter α was chosen as the 11^{th} unknown variable to detect the critical amplitude of driven force for the adding-sliding bifurcation presented in Fig. 4(d). However, these 11 equations cannot be solved analytically, and numerical methods must be applied to find their roots. Therefore, the onset condition for the adding-sliding bifurcation is semi-analytical. By solving Eqs. (43)-(53) numerically, we can obtain the values for v_1, ϕ_1, τ_1, x_2, v_2, ϕ_2, τ_2, v_3, ϕ_3, τ_3 and α, and these values determine the steady-state orbit of the system simultaneously.

5. Numerical results and discussion

As discussed before, one of the main goals in the present work is to study in detail the complex dynamics of the capsule system, with special focus on the discontinuity-induced bifurcations affecting the capsule behaviour. As part of our study, we will also investigate the effect of the control parameters on the average capsule velocity (V_{AVG}) and average power consumption (P_{AVG}) defined previously. For this purpose, we will employ specialized numerical techniques implemented via the computational platform COCO [43], so as to perform the numerical continuation and bifurcation detection of periodic solutions for the piecewise-smooth model introduced in the previous section. All computations in this section are carried out using a discretization error $\leq 10^{-6}$.

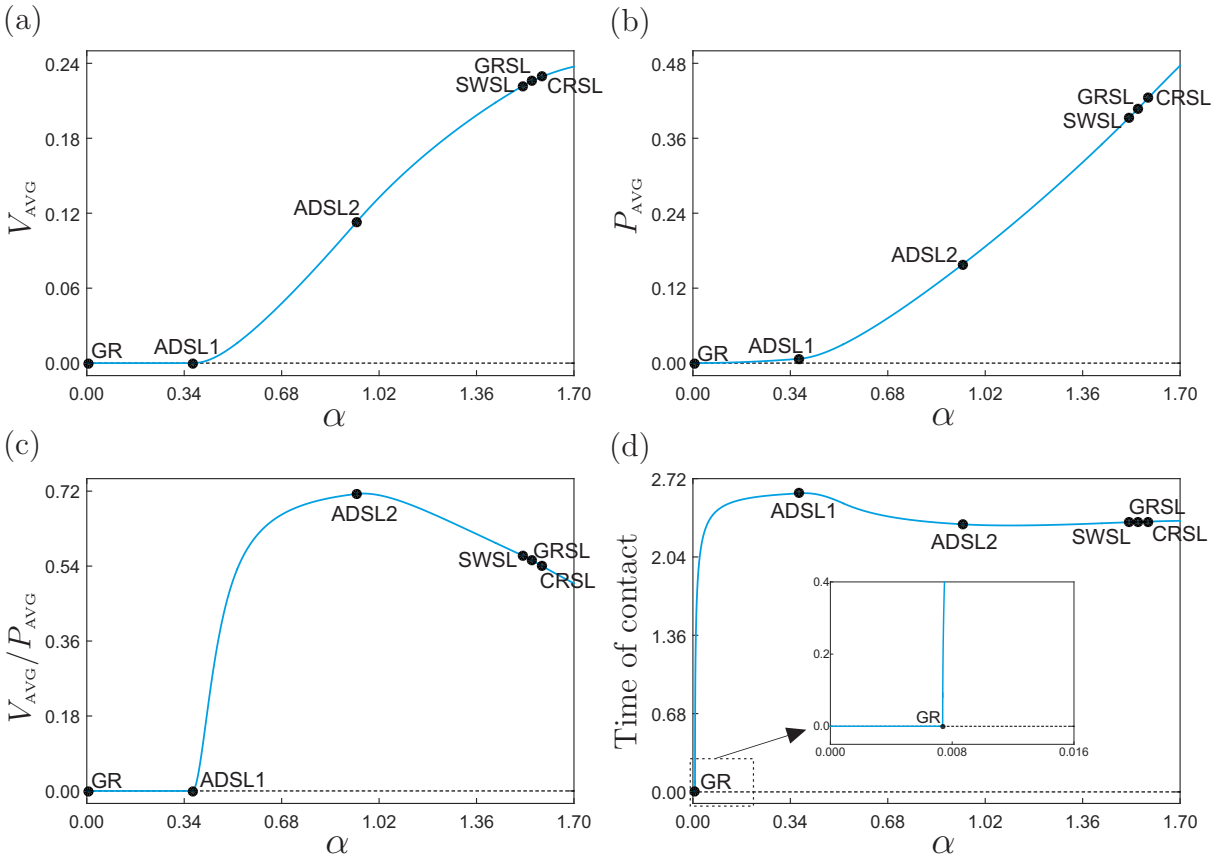

Figure 5: One-parameter continuation of the period-1 solution shown in Fig. 2 with respect to the excitation amplitude α computed for $\omega = 0.8$, $\zeta = 0.05$, $\delta = 0.02$, $\beta = 1.5$ and $\gamma = 3.3$. The pictures show the behaviour of the average capsule velocity V_{AVG} (panel (a)), average power consumption P_{AVG} (panel (b)), velocity-to-power ratio $V_{\text{AVG}}/P_{\text{AVG}}$ (panel (c)) and time of contact with the secondary spring k_2 per period (panel (d)). The points labeled GR, ADSL, SWSL, GRSL and CRSL denote grazing, adding-sliding, switching-sliding, grazing-sliding and crossing-sliding bifurcations of limit cycles.

5.1. One-parameter analysis

Our numerical study will begin with a detailed one-parameter continuation of the initial periodic solution shown in Fig. 2(a). This solution consists of 6 smooth segments given by the sequence: $I_{\text{NC-FD}}$ (*No Contact - Forward Drift*), $I_{\text{NC-ST}}$ (*No Contact - Stationary*), $I_{\text{NC-BD}}$ (*No Contact - Backward Drift*), $I_{\text{C-BD}}$ (*Contact - Backward Drift*), $I_{\text{C-ST}}$ (*Contact - Stationary*) and $I_{\text{C-FD}}$ (*Contact - Forward Drift*), starting from the reference point P (clockwise direction), see Fig. 2(a), thereby showing all the operation modes introduced in the previous section, including forward, stationary and backward motion of the capsule.

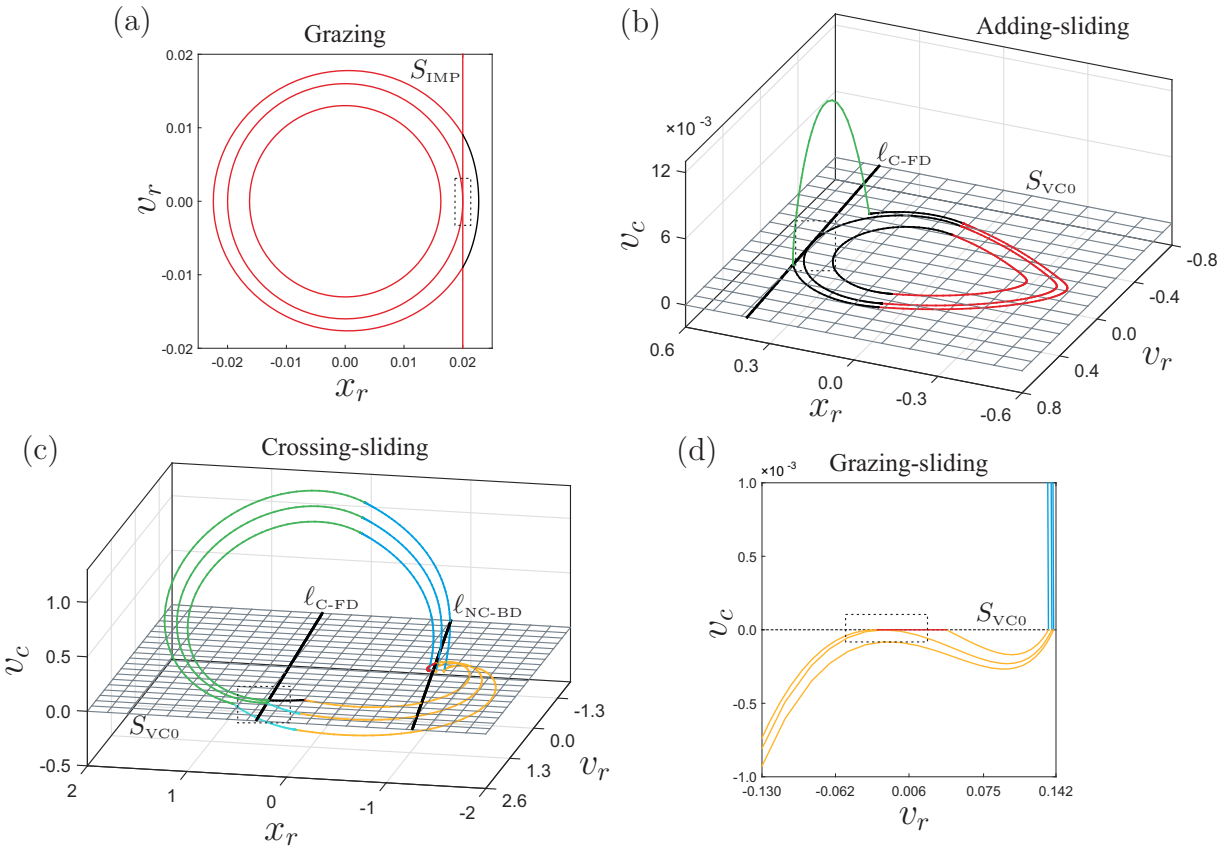

Figure 6: Phase portraits showing some of the discontinuity-induced bifurcations detected in Fig. 5 computed for $\omega = 0.8$, $\zeta = 0.05$, $\delta = 0.02$, $\beta = 1.5$ and $\gamma = 3.3$. The boxed region indicates the portion in the phase space where the bifurcation is visible. The panels also depict the discontinuity boundaries $\ell_{\text{NC-BD}}$, $\ell_{\text{C-FD}}$ and S_{VC0}, defined in Section 3.

We will now investigate via numerical continuation how the initial periodic solution displayed in Fig. 2(a) is affected when the excitation amplitude α is varied, and the other parameters of the system are kept the same as $\omega = 0.8$, $\zeta = 0.05$, $\delta = 0.02$, $\beta = 1.5$ and $\gamma = 3.3$. The result can be seen in Fig. 5, which depicts the variation effect on the average capsule velocity V_{AVG}, average power consumption P_{AVG}, velocity-to-power ratio $V_{\text{AVG}}/P_{\text{AVG}}$ and time of contact with the secondary spring k_2 per period. Starting from α close to zero, we observe that the capsule system shows periodic solutions with the internal mass oscillating without making any contact with the secondary spring k_2, due to which what is defined as 'time of contact' is zero, see Fig. 5(d). As α increases, the amplitude of oscillation also increases, until the periodic solution makes tangential contact with the impact boundary S_{IMP} ($x_r - \delta = 0$), where a grazing bifurcation GR occurs (for $\alpha \approx 0.0074$). The local behaviour around this critical point is shown in Fig. 6(a), where the capsule response before, at and after the grazing bifurcation is displayed. As can be seen, for larger values of α the internal mass now makes contact with the secondary spring, hence the time of contact increases locally after GR.

For α-values slightly larger than GR the internal mass oscillates within the capsule making intermittent contact with the secondary spring, but the capsule itself remains stationary. A critical point, however, is found at $\alpha \approx 0.3688$, where an adding-sliding bifurcation ADSL1 is detected. At this point, the periodic orbit makes tangential contact with the discontinuity boundary $\ell_{\text{C-FD}}$, which defines the threshold for the force acting on the capsule from the mass to produce forward motion of the capsule ($x_r + 2\zeta v_r + \beta(x_r - \delta) - 1 = 0$). The capsule behaviour around the critical point ADSL1 is shown in Fig. 6(b). Here, it can be seen that before the bifurcation the phase plots lie entirely on the plane S_{VC0}, where the capsule velocity is zero (i.e. $v_m - v_r = 0$). After the bifurcation, an additional operation mode $I_{\text{C-FD}}$ (*Contact - Forward Drift*, green) appears in the periodic solution, during which the capsule moves forward. Once

this solution segment terminates, the trajectory goes back to the stationary regime given by the plane S_{VC0}.

Another adding-sliding bifurcation (ADSL2) is detected for $\alpha \approx 0.9410$, as can be seen in Fig. 5. In this case, we have that before this critical point the capsule presents episodes of forward motion and zero velocity, in a typical stick-slip sequence. At the bifurcation point, the periodic orbit makes tangential contact with the discontinuity boundary $\ell_{\text{NC-BD}}$, which defines the threshold for the force acting on the capsule from the mass to produce backward motion of the capsule during the no contact mode ($x_r + 2\zeta v_r + 1 = 0$). Consequently, right after the bifurcation ADSL2 the capsule presents small regimes of backward motion whose duration locally increases when α increases. Further discontinuity-induced bifurcations are detected at $\alpha \approx 1.5218$ (switching-sliding SWSL), $\alpha \approx 1.5514$ (grazing-sliding GRSL) and $\alpha \approx 1.5886$ (crossing-sliding CRSL). The local behaviour of the capsule around some of these critical points is shown in Fig. 6.

As mentioned earlier, one of our main concerns in this numerical investigation is to identify suitable operating conditions from a practical perspective. Motivated by this goal, our numerical study includes the computation of selected solution measures, such as average capsule velocity (V_{AVG}) and average power consumption (P_{AVG}), defined previously. In Fig. 5(a) and (b) we can observe the behaviour of these quantities when the excitation amplitude α is varied. The numerical results reveal that both measures are increasing with α, which indicates that if faster forward progression is desired, then the excitation amplitude should be increased accordingly. This implies, however, also a higher energy consumption, as can be seen from the graph for P_{AVG}. Consequently, in our analysis we included a third indicator, velocity-to-power ratio ($V_{\text{AVG}}/P_{\text{AVG}}$), which can be interpreted as average capsule velocity achieved per unit of power invested, see Fig. 5(c). As can be observed in this diagram, the velocity-to-power ratio presents a maximum value for $\alpha \approx 0.9641$, after which $V_{\text{AVG}}/P_{\text{AVG}}$ steadily decreases. Therefore, from a practical perspective this would be the optimal operation point for the capsule, since the energy is employed in this case in an efficient manner.

5.2. Two- and three-parameter analysis

In the previous section we have carried out a detailed numerical study of the periodic response of the capsule model (12)–(13) subject to one-parameter variations. In this way, we have been able to accurately detect several discontinuity-induced bifurcations of limit cycles, such as grazing, adding-sliding, switching-sliding, grazing-sliding and crossing-sliding. Of particular interest is the adding-sliding bifurcation labeled ADSL1, located at $\alpha \approx 0.3688$, see Fig 6(b). As explained before, the periodic solution at this point intersects the discontinuity boundary $\ell_{\text{C-FD}}$ tangentially, which defines the threshold for the force acting on the capsule from the mass to produce forward motion of the capsule. Hence, the point ADSL1 defines a boundary between stationary and forward motion of the capsule, which can be used for control purposes in certain capsule applications. Therefore, in this section we will investigate how this critical point is affected when further system parameters are varied. Specifically, we will allow two selected parameters to vary simultaneously and trace a locus of adding-sliding bifurcations on the two-parameter plane. To this end, we will make use of COCO's functionality to impose user-defined constraints to a continuation problem, a task that can be implemented using the COCO-command 'coco_xchg_pars' [43].

The result of the process described above is shown in Fig. 7. Here, we have carried out the two-parameter continuation of the adding-sliding bifurcation ADSL1 with respect to α and β (panel (a)), α and δ (panel (b)), α and ω (panel (c)) and α and ζ (panel (d)). In all cases, the resulting curves divide the parameter space locally into two regions: one where the capsule is stationary ($V_{\text{AVG}} = 0$) and one with $V_{\text{AVG}} > 0$. The meaning of these curves is illustrated in panels (e) and (f) that depict capsule responses computed at the test points P1 ($\alpha = 0.72$, $\omega = 1.6$), P2 ($\alpha = 0.2$, $\omega \approx 1.0482$) and P3 ($\alpha = 0.3$, $\omega = 0.75$), located at the α-ω plane given in panel (c). In this way, we can determine accurately (α, ω)-values producing stationary and forward capsule motion.

Similar to the previous case where we imposed suitable constraints to the continuation problem in order to trace loci of adding-sliding bifurcations, we can use the COCO-functionality 'coco_xchg_pars' to set, for instance, average capsule velocity (V_{AVG}), average power consumption (P_{AVG}) or any other user-defined solution measure to a desired value. In particular, we will now use the continuation platform to compute families of periodic solutions with a fixed power consumption ($P_{\text{AVG}} = 0.25$) and with selected

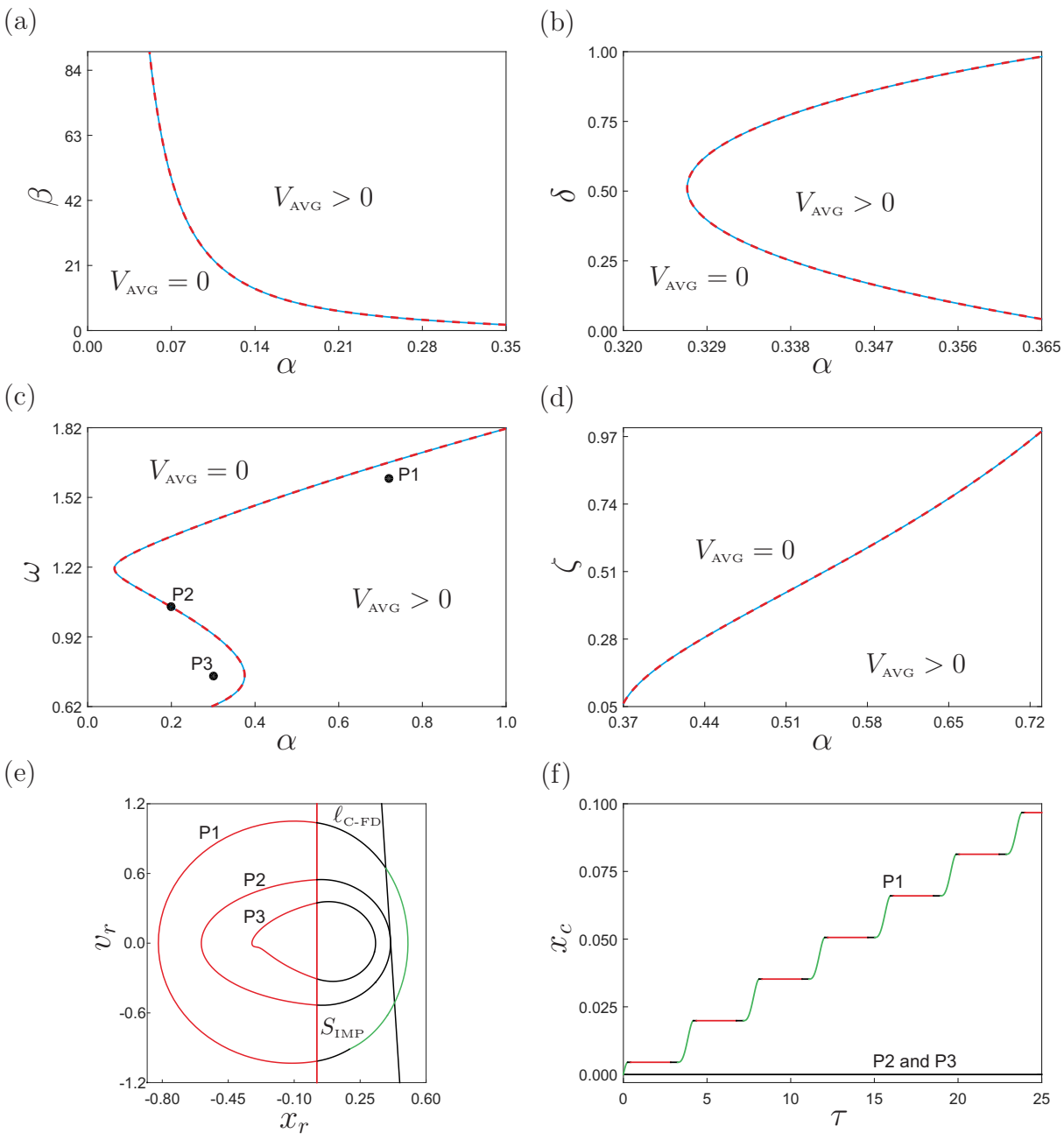

Figure 7: Two-parameter continuation of the adding-sliding bifurcation ADSL1 detected in Fig. 5 with respect to α and β (panel (a)), α and δ (panel (b)), α and ω (panel (c)) and α and ζ (panel (d)). In all cases, the curves divide the parameter space locally into two regions: one where the capsule is stationary ($V_{\mathrm{AVG}} = 0$) and one with $V_{\mathrm{AVG}} > 0$. The panels show the curves obtained numerically (in blue) and analytically (red dashed lines, see Section 4). Panels (e) and (f) present capsule responses computed at the test points P1 ($\alpha = 0.72$, $\omega = 1.6$), P2 ($\alpha = 0.2$, $\omega \approx 1.0482$) and P3 ($\alpha = 0.3$, $\omega = 0.75$), depicted in panel (c). In (e), the vertical red and inclined black lines represent the impact and friction boundaries, respectively. At the test point P2, adding-sliding bifurcation occurs. In the P2 orbit, the green segment denotes the forward motion of the capsule.

(also fixed) capsule velocities, for which we will allow three control parameters to vary (α, ω and β). The result of this process is shown in Fig. 8. Panel (a) presents the three-parameter continuation in the α-ω-β space satisfying two conditions simultaneously: $P_{\mathrm{AVG}} = 0.25$ and $V_{\mathrm{AVG}} = 0.11$ (black curve), $V_{\mathrm{AVG}} = 0.12$ (blue curve), $V_{\mathrm{AVG}} = 0.13$ (green curve), $V_{\mathrm{AVG}} = 0.14$ (red curve) and $V_{\mathrm{AVG}} = 0.15$ (yellow curve). In

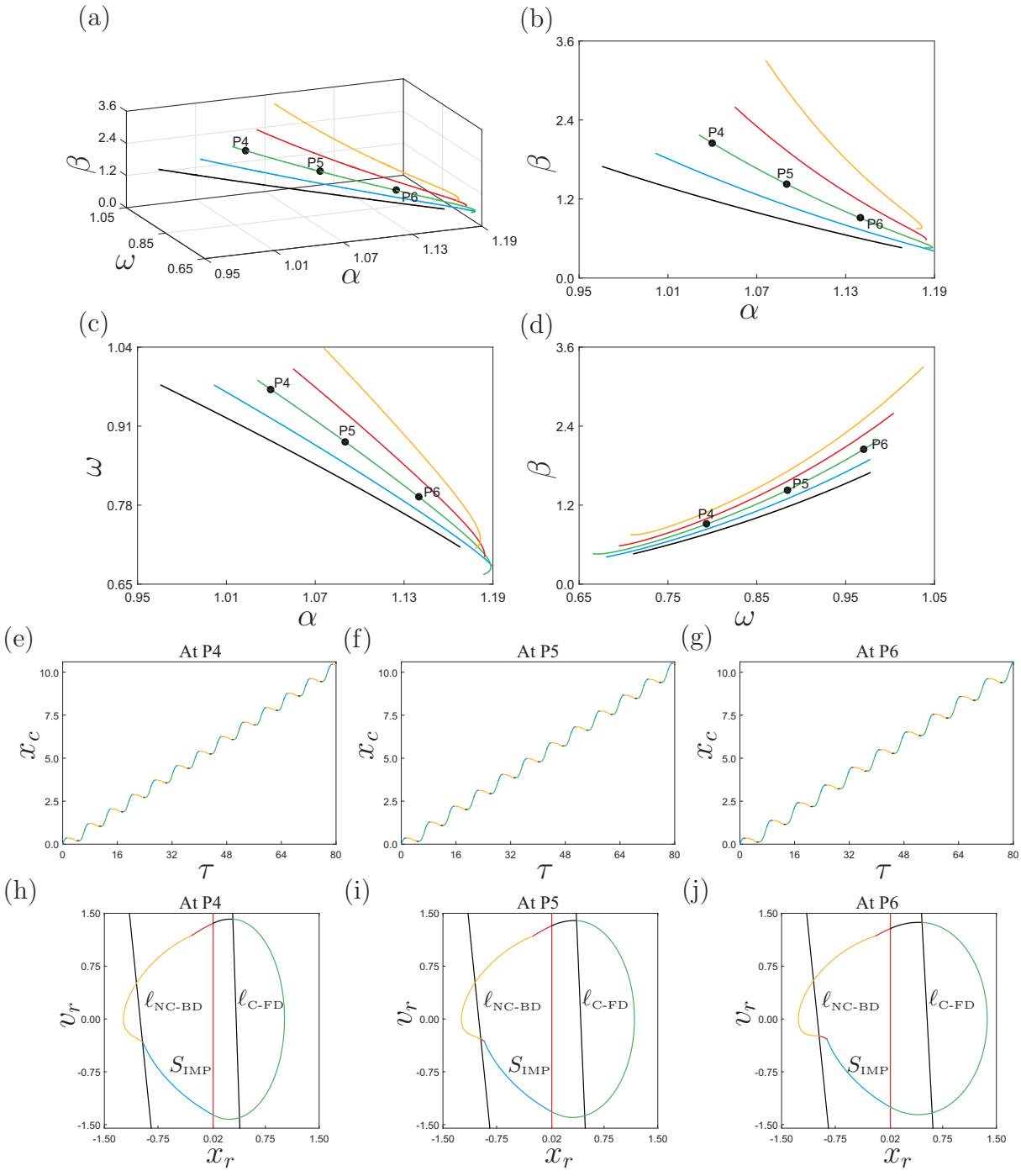

Figure 8: Three-parameter continuation of the periodic solution shown in Fig. 2 with respect to the excitation amplitude α, excitation frequency ω and stiffness ratio β. (a) Resulting curves in the α-ω-β space satisfying two conditions: $P_{\text{AVG}} = 0.25$ and $V_{\text{AVG}} = 0.11$ (black curve), $V_{\text{AVG}} = 0.12$ (blue curve), $V_{\text{AVG}} = 0.13$ (green curve), $V_{\text{AVG}} = 0.14$ (red curve) and $V_{\text{AVG}} = 0.15$ (yellow curve). Panels (b), (c) and (d) depict the projections of the computed curves onto the α-β, α-ω and ω-β planes, respectively. Panels (e)–(j) display capsule responses computed at the test points P4 ($\alpha = 1.04$, $\omega \approx 0.9706$, $\beta \approx 2.0494$), P5 ($\alpha = 1.09$, $\omega \approx 0.8846$, $\beta \approx 1.4286$) and P6 ($\alpha = 1.14$, $\omega \approx 0.7933$, $\beta \approx 0.9104$), depicted in panel (a) along the green curve (satisfying the condition $P_{\text{AVG}} = 0.25$ and $V_{\text{AVG}} = 0.13$).

this way we can accurately determine the control parameters so as to obtain a desired capsule velocity with a given power consumption. Panels (e)–(j) present capsule responses computed at the test points

P4 ($\alpha = 1.04$, $\omega \approx 0.9706$, $\beta \approx 2.0494$), P5 ($\alpha = 1.09$, $\omega \approx 0.8846$, $\beta \approx 1.4286$) and P6 ($\alpha = 1.14$, $\omega \approx 0.7933$, $\beta \approx 0.9104$), located along the green curve depicted in panel (a), satisfying the condition $P_{\text{AVG}} = 0.25$ and $V_{\text{AVG}} = 0.13$.

5.3. Semi-analytical study

For the grazing bifurcation shown in Fig. 4(b), its onset condition can be detected analytically using Eq. (28), and the analytical results are presented in Fig. 9. As shown in Fig. 9(a), the blue curve indicates the occurrence of the grazing bifurcation in the two-parameter space α-ω. The curve also divides the α-ω plane into two regions, of which the light-blue shadowed region is the subset of α-ω representing no impact in the system, while the grey shadowed region is the subset of α-ω indicating the impact between the inner mass and the capsule. The minimum driven force for grazing bifurcation is $\alpha = 0.002$, when resonance occurs at $\omega = 1$. For $\omega < 1$, the critical value of α for grazing bifurcation decreases as ω increases. On contrast, the critical value of α for grazing bifurcation increases as ω increases for $\omega > 1$. For a given set of control parameters, $\alpha = 0.0074$ and $\omega = 0.8$, the onset condition of the grazing bifurcation in the δ-ζ plane is presented in Fig. 9(b). Similarly, the parameters in the light-blue and grey shadowed areas lead to no-impact and impact motions, respectively. For the parameters on the blue curve, the value of δ decreases as ζ increases, so a small gap is required to make impact occur when the damping coefficient is large. Fig. 9(c) shows the analytical onset condition of the grazing bifurcation in the α-ζ plane with the blue and grey areas representing no-impact and impact motions, respectively. For $\omega = 0.8$ and $\delta = 0.02$, the critical value of α for impact motion increases as ζ increases indicating that a larger damping coefficient requires a larger driven force for the occurrence of impact motion.

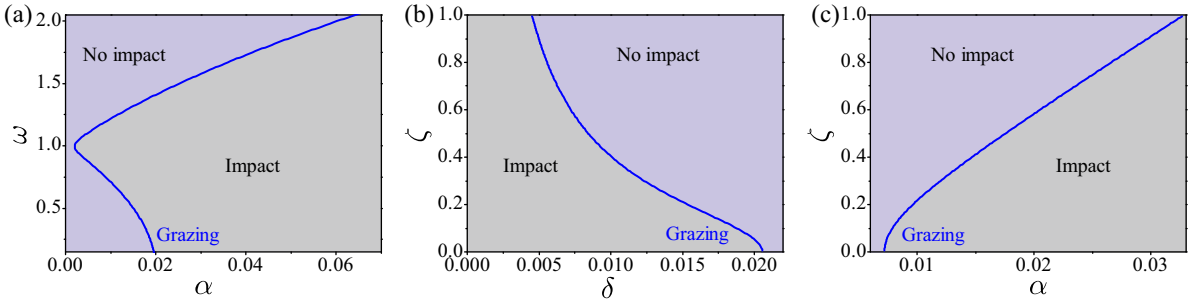

Figure 9: The grazing bifurcation shown in Fig. 4(b) detected by the analytical onset condition given by Eq. (28) in the two-parameter spaces of (a) α-ω, (b) δ-ζ and (c) α-ζ. The other parameters were calculated at $\alpha = 0.0074$, $\omega = 0.8$, $\delta = 0.02$ and $\zeta = 0.05$.

The adding-sliding bifurcation shown in Fig. 4(d) can be detected using the semi-analytical method by solving Eqs. (43)-(53). Fig. 10 illustrate the effectiveness of the proposed semi-analytical method for determining the onset conditions of such a bifurcation in two-parameter spaces. In Fig. 10, the blue curves represent the semi-analytical onset conditions of the adding-sliding bifurcation, with the grey-shadowed and green-shadowed subsets for stationary and forward-drift motions, respectively. For the given parameters $\omega = 0.8$, $\delta = 0.02$ and $\zeta = 0.05$, the critical value of α for the adding-sliding bifurcation decreases as β increases, as shown in Fig. 10(a). From the practical point of view, this means that a stiff impact spring (k_2) requires a small driven force to achieve a forward capsule motion. In Fig. 10(b), the minimum driven force for forward drift can be selected at $\alpha = 0.3269$ and $\delta = 0.51$ subjected to $\omega = 0.8$, $\beta = 1.5$, and $\zeta = 0.05$. Thus, the adding-sliding curve can be used to select the best *delta* for forward capsule motion while keeps the driven force at the minimum. The onset conditions of the adding-sliding bifurcation on the α-ω plane are presented in Fig. 10(c). As can be seen from the figure, for $\alpha \in (0.064, 0.3752)$, there exists multiple values of ω that can trigger this bifurcation. The minimal amplitude of the driven force required for forward capsule motion is $\alpha = 0.064$ at $\omega = 1.21$. In Fig. 10(d), the onset conditions on the $\alpha - \zeta$ plane is given. It can be seen from the figure that the α value on the boundary between stationary and forward-drift motions increases as ζ increases. In other words, a larger damping coefficient requires a larger driven force for forward capsule motion. Finally, these analytical

solutions were compared with the numerical results obtained by the path-following techniques in Fig. 7, which shows a good consistency.

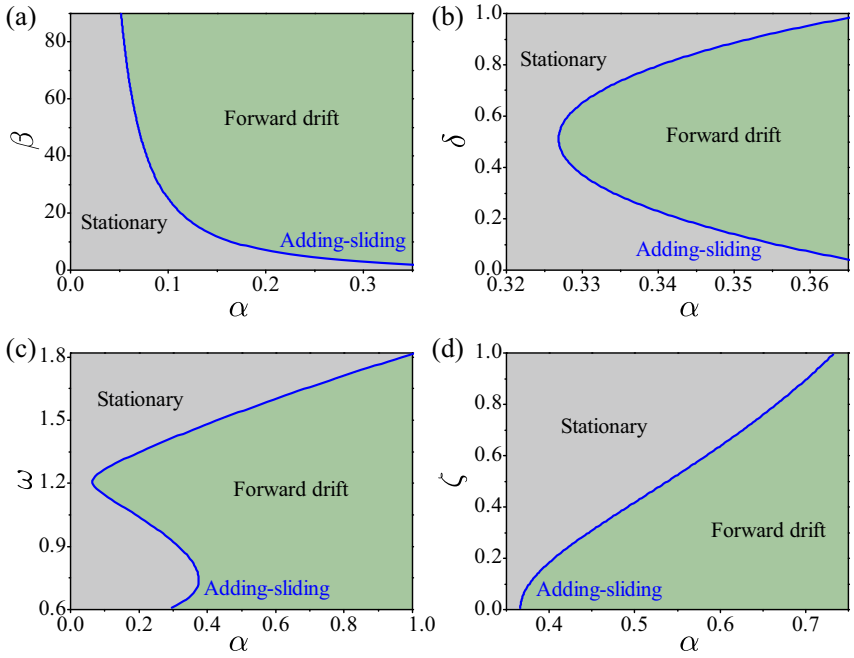

Figure 10: The adding-sliding bifurcation shown in Fig. 4(d) detected by the semi-analytical method by solving Eqs. (43)-(53) in the two-parameter spaces of (a) α-β, (b) α-δ, (c) α-ω and (d) α-ζ. The other parameters were calculated at $\alpha = 0.0074$, $\omega = 0.8$, $\beta = 1.5$, $\delta = 0.02$ and $\zeta = 0.05$.

6. Conclusions

A piecewise-smooth capsule system with bidirectional drifts was investigated in this paper via numerical and analytical approaches. The path-following techniques implemented using the continuation platform COCO were employed to detect the onset conditions of grazing and adding-sliding bifurcations, via numerical continuation in one and two parameters. These onset conditions were also derived analytically and semi-analytically, which show a good agreement with the numerical approach. The bifurcation analysis in this paper provides an in-depth understanding of the nonlinear behaviour of the piecewise-smooth capsule system when impact and friction are encountered.

The dynamics of the capsule system are characterised as piecewise-linear, which can be divided into six operation modes triggered by discrete events of impact and friction. For such a non-smooth system, the path-following techniques have shown its capacity to detect the onset conditions of some specific bifurcations as well as to optimise the progression velocity and power consumption of the system. In this study, grazing, adding-sliding, switching-sliding, grazing-sliding and crossing-sliding bifurcations were detected by varying the amplitude of the driven force α. After the occurrence of the grazing bifurcation at $\alpha \approx 0.0074$, the duration of contact between the inner mass and the secondary spring increased and then decreased after ADSL1 at $\alpha \approx 0.3688$, at where the capsule started to move forward as a whole. To evaluate the progression performance, the velocity-to-power ratio was computed by varying α, which increased after the occurrence of ADSL1 and then decreased after the onset of ADSL2 at $\alpha \approx 0.9410$. Thus, the most efficient driven force was around the critical point of ADSL2. The path-following techniques were also applied for detecting the onset conditions of ADSL1 in two-parameter spaces, which were the critical points for forward drift of the capsule. In addition, three-parameter analysis was conducted to find the parameter set to achieve a constant progression velocity by consuming a constant power. These numerical studies revealed that the optimum selection of system and control parameters can be multimodal.

On the other hand, for the grazing bifurcation, analytical onset condition was derived in Eq. (28). The occurrence of the grazing bifurcation only depends on the system parameters δ and ζ and the control parameters α and ω. According to Eq. (28), a larger damping coefficient ζ requires a smaller gap δ or a larger driven force α to satisfy the occurrence of the grazing bifurcation. In addition, a minimum driven force for grazing could only be achieved at the resonance frequency $\omega = 1$. For the adding-sliding bifurcation that leads the forward capsule motion, semi-analytical onset conditions were derived. However, the condition was implicitly contained in a group of equations in Eqs. (43)-(53), due to which a numerical method was adopted to find the roots of these equations. The onset conditions of this adding-sliding bifurcation were detected in a two-parameter space, which showed a very high consistency with the numerical results obtained by the path-following techniques. The analytical results revealed that a small driven force could result in capsule's forward drift if the secondary spring has a large stiffness k_2 or the damper had a small coefficient ζ. For minimising the driven force α around the adding-sliding bifurcation onset points, the gap δ and the driven frequency ω were obtained at $\delta \approx 0.51$ and $\omega \approx 1.21$, respectively.

Compared to the path-following techniques, the analytical approach only requires little computation resources. However, it only can detect the onset conditions of the impact-induced grazing bifurcation and the friction-induced adding-sliding bifurcation for the capsule system, while the path-following techniques are capable for detecting various bifurcation scenarios. Our future work is to derive the analytical solutions for all the six operation modes in order to analyze solutions of the capsule system undergoing more complicated bifurcation scenarios.

Acknowledgments

This work has been supported by EPSRC under Grant No. EP/P023983/1. Prof. Caishan Liu's research is supported by the National Natural Science Foundation of China under Grant No. 11932001.

Compliance with ethical standards

Conflict of interest

The authors declare that they have no conflict of interest concerning the publication of this manuscript.

Data accessibility

The datasets generated and analysed during the current study are available from the corresponding author on reasonable request.

References

[1] E. Pavlovskaia, D. C. Hendry, and M. Wiercigroch, "Modelling of high frequency vibro-impact drilling," *Int. J. Mech. Sci.*, vol. 91, pp. 110–119, 2015.

[2] M. Liao, Y. Liu, J. Páez Chávez, A. S. Chong, and M. Wiercigroch, "Dynamics of vibro-impact drilling with linear and nonlinear rock models," *Int. J. Mech. Sci.*, vol. 146, pp. 200–210, 2018.

[3] V.-D. Nguyen, K.-C. Woo, and E. Pavlovskaia, "Experimental study and mathematical modelling of a new of vibro-impact moling device," *Int. J. Nonlin. Mech.*, vol. 43, no. 6, pp. 542–550, 2008.

[4] M. A. Al-Shudeifat, N. Wierschem, D. D. Quinn, A. F. Vakakis, L. A. Bergman, and B. F. Spencer Jr, "Numerical and experimental investigation of a highly effective single-sided vibro-impact non-linear energy sink for shock mitigation," *Int. J. Nonlin. Mech.*, vol. 52, pp. 96–109, 2013.

[5] G. Pennisi, C. Stephan, E. Gourc, and G. Michon, "Experimental investigation and analytical description of a vibro-impact nes coupled to a single-degree-of-freedom linear oscillator harmonically forced," *Nonlinear Dyn.*, vol. 88, no. 3, pp. 1769–1784, 2017.

[6] D. Yurchenko, Z. Lai, G. Thomson, D. V. Val, and R. V. Bobryk, "Parametric study of a novel vibro-impact energy harvesting system with dielectric elastomer," *Appl. Energy*, vol. 208, pp. 456–470, 2017.

[7] B. Guo and J. Ringwood, "Non-linear modelling of a vibro-impact wave energy converter," *IEEE Trans. Sustain. Energy*, 2020.

[8] B. Guo, E. Ley, J. Tian, J. Zhang, Y. Liu, and S. Prasad, "Experimental and numerical studies of intestinal frictions for propulsive force optimisation of a vibro-impact capsule system," *Nonlinear Dyn.*, vol. 101, no. 1, pp. 65–83, 2020.

[9] Y. Liu, J. Páez Chávez, J. Zhang, J. Tian, B. Guo, and S. Prasad, "The vibro-impact capsule system in millimetre scale: numerical optimisation and experimental verification," *Meccanica*, vol. 55, no. 10, pp. 1885–1902, 2020.

[10] Y. Liu and J. Páez Chávez, "Controlling coexisting attractors of an impacting system via linear augmentation," *Physica D*, vol. 348, pp. 1–11, 2017.

[11] E. Pavlovskaia, M. Wiercigroch, and C. Grebogi, "Modeling of an impact system with a drift," *Phys. Rev. E*, vol. 64, no. 5, p. 056224, 2001.

[12] Y. Liu, M. Wiercigroch, E. Pavlovskaia, and H. Yu, "Modelling of a vibro-impact capsule system," *Int. J. Mech. Sci.*, vol. 66, pp. 2–11, 2013.

[13] A. B. Nordmark, "Non-periodic motion caused by grazing incidence in an impact oscillator," *J. Sound Vib.*, vol. 145, no. 2, pp. 279–297, 1991.

[14] S. Yin, J. Ji, S. Deng, and G. Wen, "Degenerate grazing bifurcations in a three-degree-of-freedom impact oscillator," *Nonlinear Dyn.*, vol. 97, no. 1, pp. 525–539, 2019.

[15] Z. Zhang, Y. Liu, and J. Sieber, "Calculating the Lyapunov exponents of a piecewise smooth soft impacting system with a time-delayed feedback controller," *Comm. Nonlinear Sci. Numer. Simulat.*, vol. 91, p. 105451, 2020.

[16] Z. Du, H. Fang, X. Zhan, and J. Xu, "Experiments on vibration-driven stick-slip locomotion: A sliding bifurcation perspective," *Mech. Syst. Signal Process.*, vol. 105, pp. 261–275, 2018.

[17] M. Di Bernardo, P. Kowalczyk, and A. Nordmark, "Bifurcations of dynamical systems with sliding: derivation of normal-form mappings," *Physica D*, vol. 170, no. 3-4, pp. 175–205, 2002.

[18] J.-H. Ho, V.-D. Nguyen, and K.-C. Woo, "Nonlinear dynamics of a new electro-vibro-impact system," *Nonlinear Dyn.*, vol. 63, no. 1-2, pp. 35–49, 2011.

[19] T.-H. Duong, V.-D. Nguyen, H.-C. Nguyen, N.-P. Vu, N.-K. Ngo, and V.-T. Nguyen, "A new design for bidirectional autogenous mobile systems with two-side drifting impact oscillator," *Int. J. Mech. Sci.*, vol. 140, pp. 325–338, 2018.

[20] Y. Liu and J. Páez Chávez, "Controlling multistability in a vibro-impact capsule system," *Nonlinear Dyn.*, vol. 88, no. 2, pp. 1289–1304, 2017.

[21] Y. Zhang and G. Luo, "Multistability of a three-degree-of-freedom vibro-impact system," *Comm. Nonlinear Sci. Numer. Simulat.*, vol. 57, pp. 331–341, 2018.

[22] A. C. Luo and R. P. Han, "The dynamics of a bouncing ball with a sinusoidally vibrating table revisited," *Nonlinear Dyn.*, vol. 10, no. 1, pp. 1–18, 1996.

[23] S. Yin, Y. Shen, G. Wen, and H. Xu, "Analytical determination for degenerate grazing bifurcation points in the single-degree-of-freedom impact oscillator," *Nonlinear Dyn.*, vol. 90, no. 1, pp. 443–456, 2017.

[24] G. Luo, J. Xie, and S. Guo, "Periodic motions and global bifurcations of a two-degree-of-freedom system with plastic vibro-impact," *J. Sound Vib.*, vol. 240, no. 5, pp. 837–858, 2001.

[25] T. Li, E. Gourc, S. Seguy, and A. Berlioz, "Dynamics of two vibro-impact nonlinear energy sinks in parallel under periodic and transient excitations," *Int. J. Nonlin. Mech.*, vol. 90, pp. 100–110, 2017.

[26] E. Gourc, G. Michon, S. Seguy, and A. Berlioz, "Targeted energy transfer under harmonic forcing with a vibro-impact nonlinear energy sink: analytical and experimental developments," *J. Vib. Acoust.*, vol. 137, no. 3, 2015.

[27] A. C. Luo, "Period-doubling induced chaotic motion in the lr model of a horizontal impact oscillator," *Chaos Soliton. Fract.*, vol. 19, no. 4, pp. 823–839, 2004.

[28] E. Pavlovskaia and M. Wiercigroch, "Analytical drift reconstruction for visco-elastic impact oscillators operating in periodic and chaotic regimes," *Chaos Soliton. Fract.*, vol. 19, no. 1, pp. 151–161, 2004.

[29] E. Pavlovskaia and M. Wiercigroch, "Low-dimensional maps for piecewise smooth oscillators," *J. Sound Vib.*, vol. 305, no. 4-5, pp. 750–771, 2007.

[30] H. Fang and J. Xu, "Stick-slip effect in a vibration-driven system with dry friction: sliding bifurcations and optimization," *J. Appl. Mech.*, vol. 81, no. 5, 2014.

[31] B. J. Nelson, I. K. Kaliakatsos, and J. J. Abbott, "Microrobots for minimally invasive medicine," *Annu. Rev. Biomed. Eng*, vol. 12, pp. 55–85, 2010.

[32] F. L. Chernous'ko, "The optimum rectilinear motion of a two-mass system," *J. Appl. Math.*, vol. 66, no. 1, pp. 1–7, 2002.

[33] F. L. Chernous'ko, "Analysis and optimization of the motion of a body controlled by means of a movable internal mass," *J. Appl. Math.*, vol. 70, no. 6, pp. 819–842, 2006.

[34] Y. Liu, E. Pavlovskaia, D. Hendry, and M. Wiercigroch, "Vibro-impact responses of capsule system with various friction models," *Int. J. Mech. Sci.*, vol. 72, pp. 39–54, 2013.

[35] Y. Yan, Y. Liu, L. Manfredi, and S. Prasad, "Modelling of a vibro-impact self-propelled capsule in the small intestine," *Nonlinear Dyn.*, vol. 96, no. 1, pp. 123–144, 2019.

[36] B. Guo, Y. Liu, and S. Prasad, "Modelling of capsule–intestine contact for a self-propelled capsule robot via experimental and numerical investigation," *Nonlinear Dyn.*, vol. 98, no. 4, pp. 3155–3167, 2019.

[37] Y. Liu, E. Pavlovskaia, and M. Wiercigroch, "Experimental verification of the vibro-impact capsule model," *Nonlinear Dyn.*, vol. 83, no. 1-2, pp. 1029–1041, 2016.

[38] Y. Liu, E. Pavlovskaia, M. Wiercigroch, and Z. Peng, "Forward and backward motion control of a vibro-impact capsule system," *Int. J. of NonLin. Mech.*, vol. 70, pp. 30–46, 2015.

[39] B. Guo, Y. Liu, R. Birler, and S. Prasad, "Self-propelled capsule endoscopy for small-bowel examination: Proof-of-concept and model verification," *Int. J. Mech. Sci.*, vol. 174, p. 105506, 2020.

[40] M. di Bernardo, C. J. Budd, A. R. Champneys, and P. Kowalczyk, *Piecewise-smooth dynamical systems. Theory and Applications*, vol. 163 of *Applied Mathematical Sciences*. New York: Springer-Verlag, 2004.

[41] F. Dercole and Y. A. Kuznetsov, "SlideCont: An Auto97 Driver for Bifurcation Analysis of Filippov Systems," *ACM Trans. Math. Software*, vol. 31, no. 1, pp. 95–119, 2005.

[42] P. Thota and H. Dankowicz, "TC-HAT: A Novel Toolbox for the Continuation of Periodic Trajectories in Hybrid Dynamical Systems," *SIAM J. Appl. Dyn. Sys.*, vol. 7, no. 4, pp. 1283–1322, 2008.

[43] H. Dankowicz and F. Schilder, *Recipes for continuation*. Computational Science and Engineering, Philadelphia: SIAM, 2013.

[44] B. Guo and Y. Liu, "Three-dimensional map for a piecewise-linear capsule system with bidirectional drifts," *Physica D*, vol. 399, pp. 95–107, 2019.

[45] J. Páez Chávez, Y. Liu, E. Pavlovskaia, and M. Wiercigroch, "Path-following analysis of the dynamical response of a piecewise-linear capsule system," *Comm. Nonlinear Sci. Numer. Simulat.*, vol. 37, pp. 102–114, 2016.

[46] B. Krauskopf, H. Osinga, and J. Galán-Vioque, eds., *Numerical Continuation Methods for Dynamical Systems*. Understanding Complex Systems, Netherlands: Springer-Verlag, 2007.